Approved: _____

Steven A. Ackerman

Professor, Department of Atmospheric and Oceanic Sciences

Date: _____

Approved: _____

Justin M. Sieglaff

Science Advisor, UW-CIMSS

Date: _____

INTERPRETATION OF SMALL PARTICLE SIGNATURES IN SATELLITE OBSERVATIONS OF CONVECTIVE STORMS

By
Caitlin J Hart

A thesis submitted in partial fulfillment of the requirements for the degree of

MASTER OF SCIENCE
(ATMOSPHERIC AND OCEANIC SCIENCE)
at the
UNIVERSITY OF WISCONSIN-MADISON
2012

Acknowledgements

Thanks to Andi Walther and Andrew Heidinger at NESDIS for providing assistance with the application of the DCOMP algorithm.

Valuable advice was also provided by Pao Wang, Steve Ackerman and Wayne Feltz and Kai-Yuan Cheng during the design and execution of the methodology.

Funding for this research was provided by the CIMSS Cooperative Agreement grant NA10NES4400013

Satellite data was provided by the Space Science and Engineering datacenter and the radar data was provided by the University of Oklahoma/National Severe Storms Laboratory.

Thank you to Justin Sieglaff for advising this project and providing indispensable guidance, expertise and encouragement during the research process.

Abstract

This project used the Daytime Cloud Optical Microphysical Properties (DCOMP) retrieval applied to GOES-12 data to study the relationship between regions in convective anvils, associated with convective updraft cores, where the effective radius is significantly smaller than the surrounding anvil.

Small particle signatures (SPS) are defined as regions of at least two pixels where the effective radius is generally 20 μm or less, and nearby anvil effective radius retrievals are 24 μm – 30 μm or greater, and are located in the coldest (<= 215 K) region of the anvil, as identified by GOES-12 10.7 μm brightness temperature. A total of 343 SPS were manually identified in GOES imagery. Validation was performed by comparing SPS to 30 dBZ Echo Top Height (ETH) data. From this analysis, we confirmed that SPS are caused by strong updrafts, as determined by 30 dBZ ETH, and occur shortly after intensification of the updraft.

Without access to radar, the identification of an SPS could be used to identify regions where a strong updraft has recently emerged or strengthened. This could be very useful for aviation weather monitoring over ocean areas. Avenues of future work are suggested which would be necessary for moving these findings closer to operational usability.

Table of Contents

I. Introduction

In the United States, severe weather is responsible for billions of dollars in damage to property and agriculture and hundreds of deaths (National Weather Service Weather Fatality, Injury and Damage Statistics). Strong convection can produce hazards including strong wind, tornados, heavy precipitation and hail. These hazards are enabled by the dynamics within the storm's core. The most extreme example of strong convection, the supercell, develops a tilted, rotating updraft, which avoids precipitation loading and allows for a long lived storm (Ludlam, 1963). The large scale rotation, if accompanied by strong low-level directional wind shear, can support the formation of tornadoes (Moller, et al. 1994). The speed of the updraft, often in excess of 30 m/s, can support large particles aloft, resulting in the growth of hail in excess of 1" (NWS JetStream, 2011). Other types of organized convection, such as squall lines and multi-cell convective complexes, are also capable of producing severe weather. Gust fronts, originating from strong downdrafts as the storm decays, can interact with the surface cold pool and combine with instability in the surrounding environment and cause new cells to arise over the same area (Mueller and Carbone, 1987). Multiple storms training over a region will result in an increased risk of flooding due to the steady, long-lived, precipitation (Glossary, NWS). For these reasons, it is important to identify potentially severe convection as early as possible. Working toward this goal, many research projects that utilize remote sensing observations have shown great success in improving the detection of these hazardous storms.

The introduction of the NEXRAD WSR-88D radar network contributed significantly to increased warning lead times and better understanding of convective storms (Polger et al., 1994; Bieringer and Ray, 1996). Radar is used extensively by operational forecasters to issue

severe storm warnings and by the research community to understand the storm lifecycle. Rainfall estimates are a prime example of improvements in weather forecasting contributed by remote sensing data (Fulton, et al., 1998). Radial and storm relative velocity measurements have helped researchers understand storm motion and assess the threat of tornadoes and damaging straight line winds (Ryzhkov, et al., 2005; Sun and Zhang, 2008).

Satellite observations have also enabled researchers to study severe weather by observing how changes at the cloud top indicate potential for, or ongoing, severe convection. For example, the University of Wisconsin Convective Initiation algorithm (Sieglaff, et al., 2011) is an example of using satellite-detected cloud-top brightness temperature changes to estimate the growth rate of new convection. Rapidly decreasing temperatures indicate a rapidly growing updraft resulting in intense precipitation and, given favorable meteorological conditions, severe weather. Overshooting tops can be identified in visible (VIS) imagery as well as identified as exceptionally cold, isolated, cloud tops in the infrared (IR) (Bedka, et al., 2010). Overshooting tops are known to be associated with strong updrafts and severe storms (Dworak et al., 2012). The reflectance of ice and water cloud particles in the near-infrared (NIR) has been used to assess particle size in the anvils of severe convection. Smaller particles are highly reflective in the NIR, so reflectivity at these wavelengths is used as a proxy for cloud particle size. It was established that convective regions from the Great Plains to the Pacific coast have a smaller average cloud particle size than convective regions further east (Lindsey, et al., (2006), Lindsey and Grasso, (2008)). Recently, the impetus to develop products for the future GOES-R Advanced Baseline Imager (ABI) has resulted in a new daytime microphysical properties retrieval which can be executed using one VIS channel and one of three NIR channels.

The Daytime Cloud Optical Microphysical Properties (DCOMP) retrieval was developed by (Walther, et al., 2010). The retrieval uses the 0.6 μm VIS band and one of three weakly absorbing NIR bands, 1.6 μm, 2.2 μm or 3.75 μm. This flexibility enables the retrieval algorithm to be applied to data from multiple satellite sensors, in both geostationary and low-earth orbit, (e.g - GOES, VIIRS, AVHRR, MODIS, etc.) (Walter, et al., 2012). Liquid water and ice have different absorption properties in the NIR and particle size has a strong effect on scattering in the VIS (Rockel, Raschke, and Weyres, 1991). DCOMP leverages these radiative properties to derive cloud ice/water path, cloud optical depth and effective radius. The technical specification of the algorithm will be discussed in depth in Section 2.

In general, the storm anvil top consists of relatively large ice aggregates (Fulton and Haymsfield, 1991) and the edges dissolve into an extensive wispy cirrus field which consists of small, semi-transparent, ice crystals. Updrafts strong enough to produce severe weather or break the thermal cap at the tropopause may have different microphysical characteristics than the surrounding anvil (Lindsey and Grasso, 2008). This study investigates compact regions of retrieved effective radius that are significantly smaller than the surrounding anvil. Specifically, DCOMP effective radius retrievals and NEXRAD radar observations are used to study the association between the updraft core of strong convection and regions of small effective radius. In this study we seek to establish 1) the frequency with which these small particle regions are collocated with updraft cores in NEXRAD observations and 2) the temporal lag of the appearance of a small particle region relative to the most rapid increase in NEXRAD observed 30 dBZ Echo Top Height.

This paper is organized in five sections. Section 2 presents a review of the literature related to storm dynamics and microphysics, and a complete overview of the DCOMP effective radius retrieval. Section 3 introduces the data and the methodology used to establish the relationship between small effective radius regions and strong updrafts. Section 4 comprises the results, analysis and a discussion of error contributions. Section 5 presents the conclusions and summarizes beneficial expansions on this work for future consideration.

II. Background

A. Dynamics of an updraft

Multiple environmental factors contribute to severe convection. The structure of the updraft is one of the most important considerations, as it determines the lifetime of the storm. In an environment with strong vertical wind speed shear, the updraft becomes tilted (Figure 1). This greatly extends the life of the storm, because the precipitation does not fall directly into the updraft and the warm air intake can continue (Ludlam, 1963). The tilted updraft is a common feature associated with all types of severe convection, from discrete cells to organized convective complexes (Doswell, 2001).

Figure 1: In an environment with strong vertical speed shear, the updraft becomes tilted, separating the precipitation core from the warm are intake. (National Weather Service/Southern Region Headquarters)

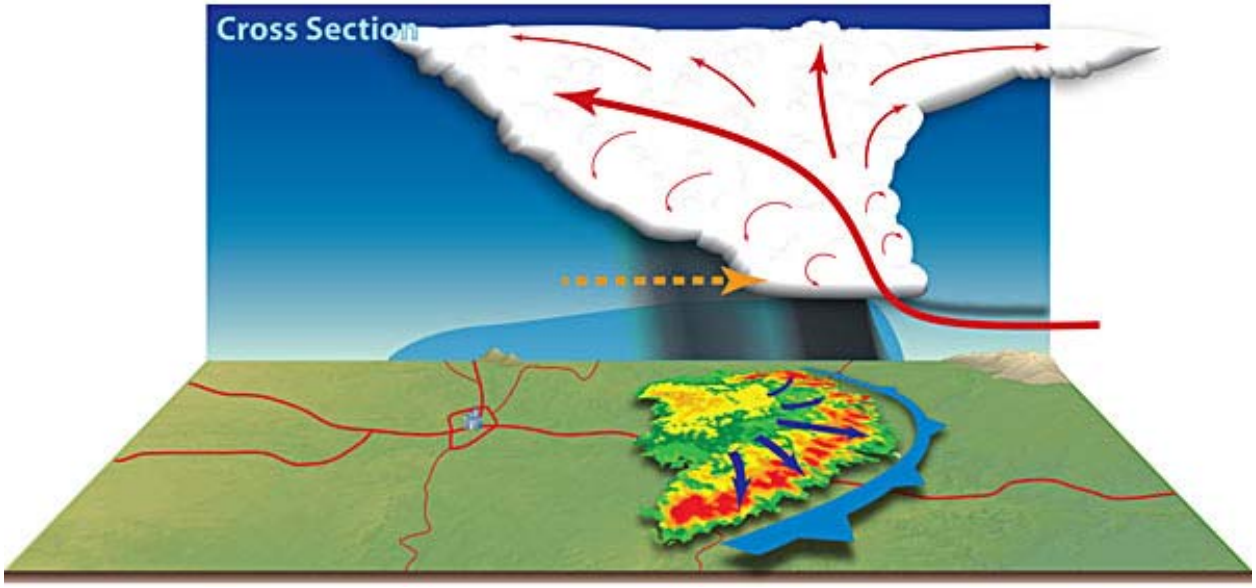

While structure contributes to the longevity of a storm, it is the mesoscale and synoptic scale thermodynamic environment which contributes to the strength of the updraft. Conditional instability, in the form of dry, cold air aloft and warm, moist air near the Earth's surface largely dictates potential updraft strength (Doswell, 2001). The intensity of the horizontal thermodynamic boundaries provides a mechanism to trigger thunderstorm development. Cold fronts and drylines are two examples of strong horizontal gradients of temperature and moisture, respectively. An example of a dryline setup is shown in Figure 2. Significant amounts of convective available potential energy (CAPE), in a vertically constrained region above the thermal cap, provides the thermodynamic environment favorable for deep, explosive convection, once the cap has been broken via a forcing mechanism (e.g. frontal passage) or convection from the ground warming through the day (Doswell, 1987).

Figure 2: A dryline set up over Kansas and Oklahoma on April 27, 2012. Note the 30 C drop in dew point temperatures between Oklahoma City (61 C) and Hobart, OK (33 C), a distance of 149 km. (Grams, SPC, 2012)

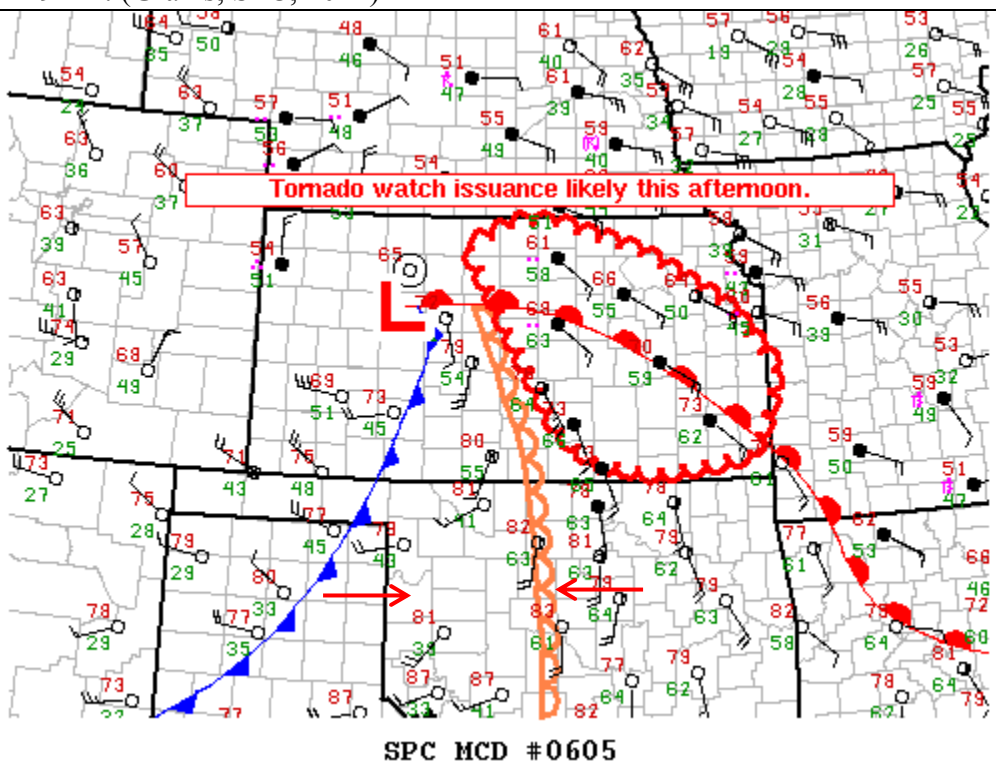

Once the updraft is formed, it ascends with tremendous upward force. The momentum of the updraft is sometimes great enough that the updraft will continue past the equilibrium level (EL) until it has moved through an area of negative CAPE equal to the positive CAPE between the level of free convection (LFC) and the EL. The top of this region of negative CAPE is the maximum parcel level (MPL) and it indicates the maximum height of an overshooting top over an anvil at the EL (Figure 3). A greater distance between the EL and MPL indicates a stronger updraft (Edwards and Thompson, 2000). A discussion of storm top cloud microphysics associated with these strong convective updrafts is presented in the following sub-section.

Figure 3: This is an example of a thermodynamic diagram indicating the dew point (dashed red line), temperatures (solid red line), CAPE (shaded red) and negative cape (shaded teal). (National Weather Service Forecast Office, Columbia, SC). The LFC, EL and MPL are indicated.

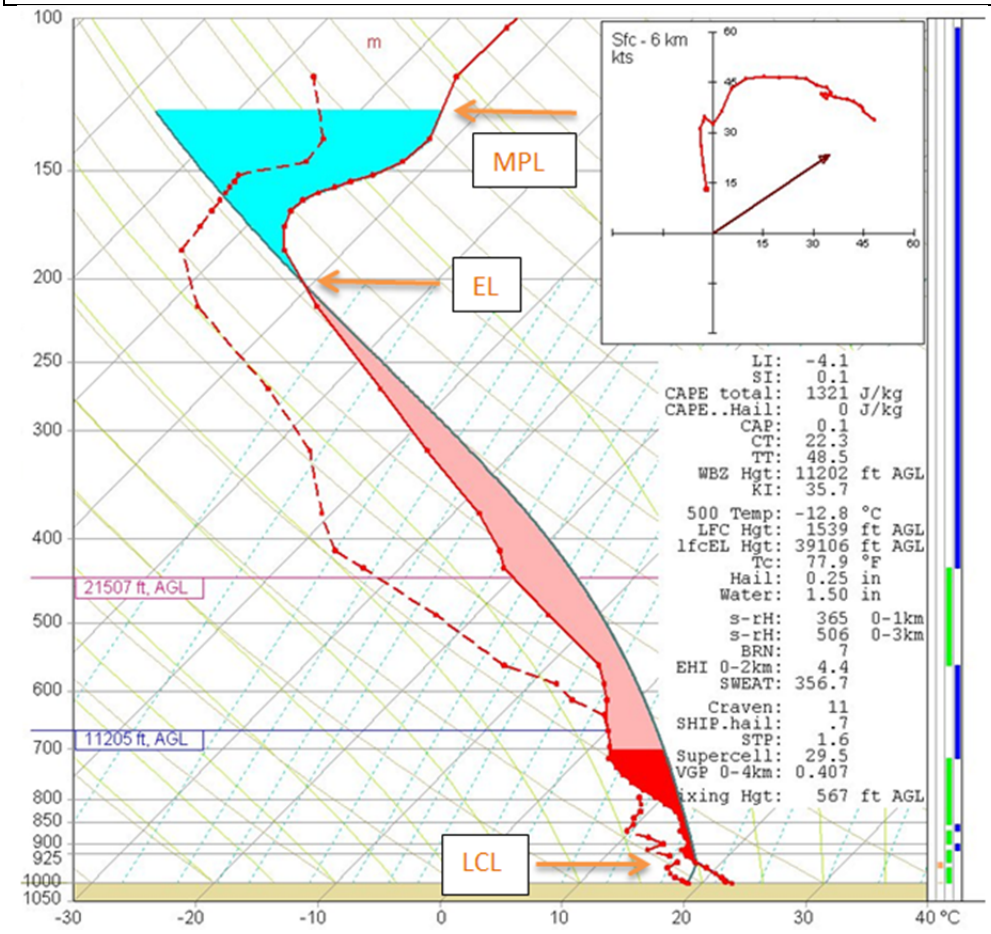

B. Microphysics Literature Review

Strong updrafts drive the vertical distribution of cloud particle sizes and cloud particle phase (liquid, supercooled, or frozen). In Rosenfeld and Woodley (2000), supercooled water droplets with a mean volume diameter of 17 μm were observed at temperatures as low as -35.7 C, with the concentration of supercooled liquid water content (SLWC) falling to near zero at temperatures slightly below, suggesting rapid homogeneous freezing around that level. Khain, Rosenfeld and Pokrovsky (2001) enumerated a number of reasons why SLWC

can exist at such low temperatures, for example, due to the small size of the drops, freezing by contact or immersion is negligible because the collision efficiency of small ice particles is extremely low. Small graupel particles do not collect droplets less than 10 μm. Due to the flow of air around a small droplet or ice particle, smaller particles are swept around the collector, rather than colliding with it. Given that there is no efficient mechanism available to facilitate freezing of very small supercooled water droplets until homogeneous freezing takes over. The stronger the upward vertical force, the higher these small droplets will be propelled in the cloud. The strongest updrafts loft these small particles to cloud-top , which can be identified within satellite observations.

Kain, Rosenfeld and Pokrovsky (2001) and Rosenfeld and Woodley (2000) observed high concentrations of SLWC in convective storms in both mid-latitude and tropical locations. In a field campaign in Thailand SLWC of 2.4 g m^{-3} was observed at -31.6 C. This was the operational ceiling of the aircraft but, in a later field campaign over Texas, similar concentrations were observed at temperatures at -35.7 C (Rosenfeld and Woodley, 2000). Though not investigated, both of these studies hypothesized that an increased availability of aerosol cloud condensation nuclei (CCN) may also contribute to higher concentrations of smaller drop sizes. The effect of aerosols on microphysics can be seen in 'ship tracks' in marine stratiform cloud layers. The exhaust from the ships provides locally higher concentrations of CCN, resulting in smaller sized drops which are more reflective in the NIR (King et al., 1989)

The effect of CCN availability and size of cloud top effective radius has been studied using satellite technology by Rosenfeld and Lensky, 1998. Using red/blue/green (RBG) composites of Advanced Very High Resolution Radiometer (AVHRR) images over marine,

continental and transition environments this study shows that continental clouds have a large diffusional growth zone, with the effective radius growing very slowly with decreasing temperature (used by Rosenfeld and Lensky as a proxy for height). A stronger updraft would exacerbate this effect (Lindsey, et al., 2006), resulting in smaller particles at the cloud top in the region of the updraft.

Lindsey, et al. (2006) closely examined strong convection over the United States using the GOES 3.9 μm reflectivity as a proxy for effective radius. Nakajima and King (1990) showed that for optically thick clouds, the reflectivity of the NIR absorption wavelengths is a function of particle size and not optical depth (τ) (Figure 4). The study used climatological average of GOES 3.9 μm reflectivity in 1 x 1 degree boxes to show conclusively that high reflectivity in this band is correlated with highly unstable environments, which support strong updraft development. Table 1 and Figure 5 show a comparison between highly reflective convective storms and non-reflective storms. The reflective storms have a significantly steeper 800-500 hPa lapse rate, drier layer aloft at 700 hPA, and greater surface-500 hPa zonal shear then the non-reflective storms. These conditions support stronger, more organized, updrafts, which contribute to the higher 3.9 μm reflectivity. As such, this study focuses on strong convective cases (e.g. those storms associated with severe weather reports).

Figure 4: From Nakajima and King (1990), this figure shows that reflectance in the NIR is only a function of effective radius for cloud optical depths greater than 16. The solid curves represent different effective radius values and the dashed lines represent different cloud optical depth values.

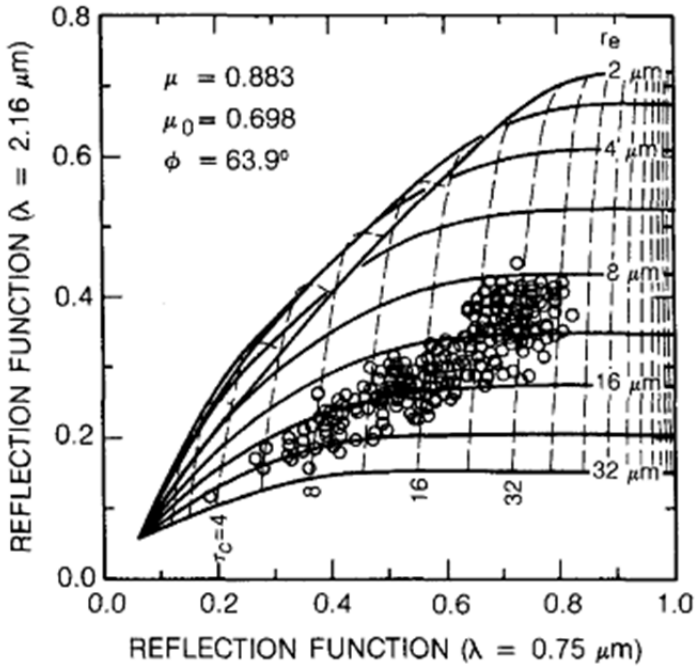

Table 1: Table 2 from (Lindsey, et al. 2006) contrasts several storm and environmental properties which differed between highly reflective days and non-reflective days. The bolded and italic numbers are properties where the difference of means exceeds 99% and 95% significance, respectively.

Parameter	Reflective case mean	Nonreflective case mean
CAPE (J kg^{-1})	*567*	*219*
Precipitable water (mm)	**17.7**	**23.1**
Surface temperature (°C)	28.2	26.1
Surface dewpoint (°C)	*4.5*	*7.2*
700-hPa RH (%)	**42**	**56**
500-hPa RH (%)	58	65
800–500-hPa lapse rate (°C km^{-1})	**8.5**	**7.4**
Surface–500-hPa zonal shear (m s^{-1})	**9.9**	**2.3**
Depth of cloud base to −38°C level (m)	*5210*	*6036*

Figure 5: In these scenes, GOES-12 3.9 µm reflectivity is superimposed over regions where GOES-12 10.7 µm brightness temperature is less than -40 C. Scene a) shows a highly reflective scene and b) a non- reflective scene. (Figure 1, Lindsey, et al. 2006)

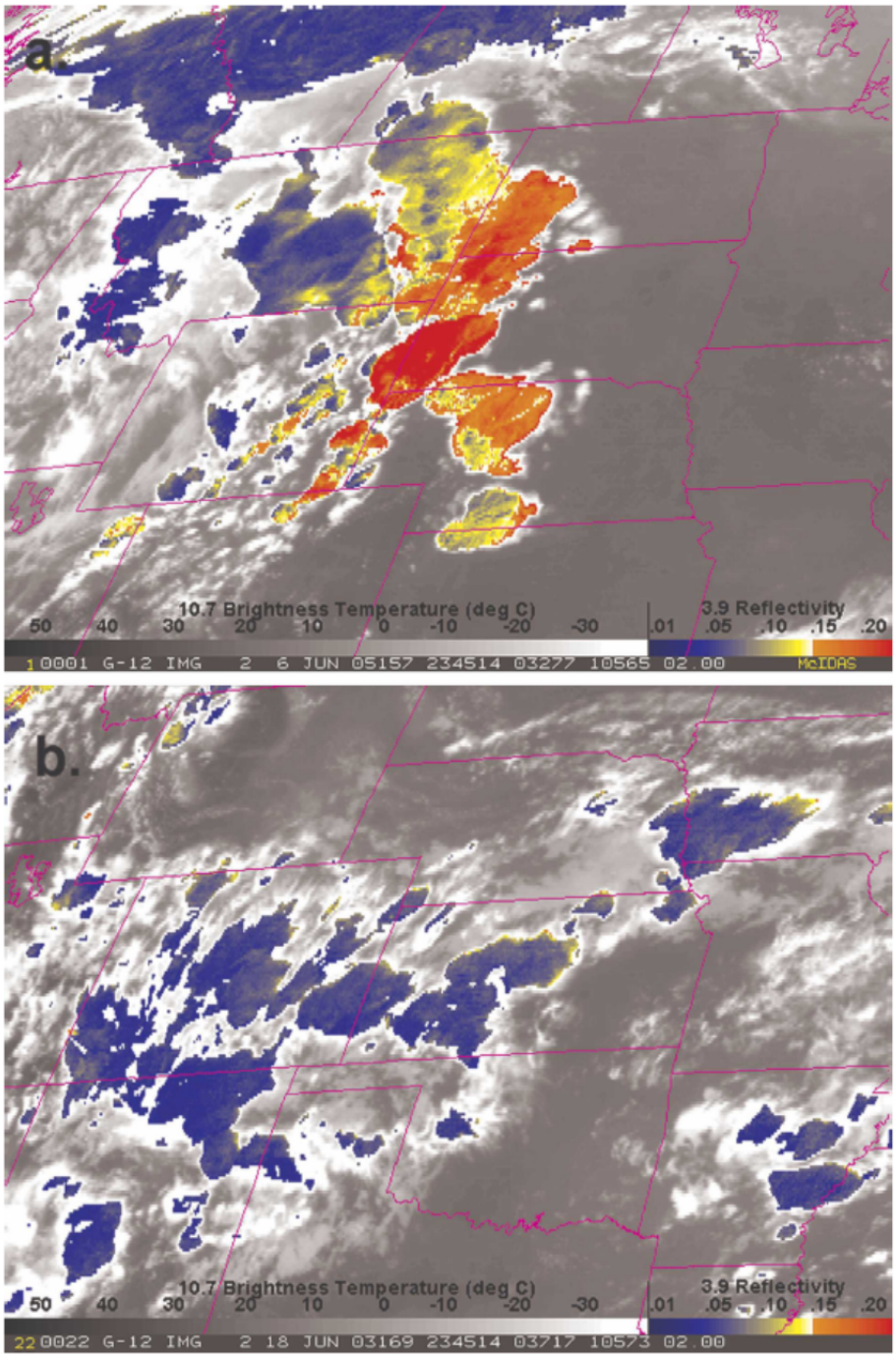

Building up on the study by Lindsey et al. (2006), Lindsey and Grasso (2008) developed an algorithm for GOES to retrieve effective radius using the VIS channel, 3.9 μm channel and the 10.7 μm channel. The VIS channel is used to select cloud regions of optical thickness sufficient to avoid transmission from below ($\tau > 20$) and the 10.7 μm channel is used to derive reflectivity at 3.9 μm. A forward model using the Spherical Harmonic Discrete Ordinate Method (SHDOM; Evans, 1998) is used to populate a lookup table of expected 3.9 μm reflectivity. Figure 6 shows an example of Lindsey and Grasso (2008) retrieval applied to a GOES image. Though they did not pursue this line of inquiry, note the highlighted regions of smaller effective radius in the storm anvils. In the next sections, the DCOMP effective radius retrieval and NEXRAD radar observations are used to investigate the association between these small particle regions and the core updraft of the storm. The next section presents an overview of DCOMP.

Figure 6: An example of the effective radius retrieval developed by Lindsey and Grasso, 2008. Note the small regions of smaller effective radius in the storm anvil over Iowa.

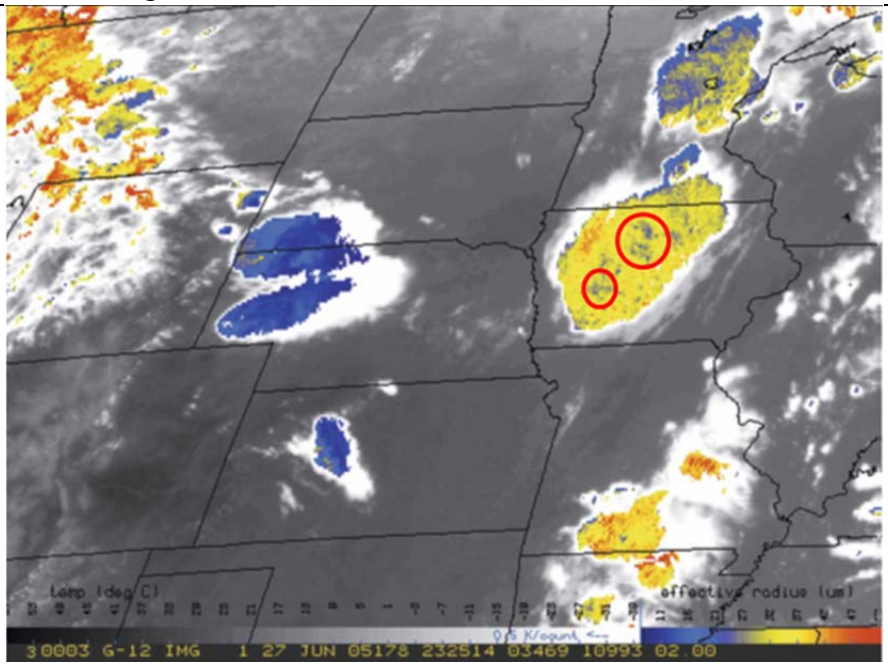

C. Technical Overview of DCOMP

DCOMP returns three microphysical parameters, optical depth (τ), effective radius (r_e) and liquid or ice water path (LWP/IWP).

Optical depth is defined as:

$$\tau = \int n(r)Q(r,\lambda)\pi r^2 dr \tag{1}$$

Where n(r) is the drop size distribution and Q is the scattering coefficient. Effective radius, the property used in this study, is defined as the ratio of the third moment to the second moment of the drop size distribution (Hansen and Travis, 1974).

$$r_e = \frac{\int r^3 n(r) dr}{\int r^2 n(r) dr} \tag{2}$$

Liquid and ice water path are defined as in (Bennartz, 2007), and (Heymsfield, 2003), respectively.

$$\text{LWP} = \frac{5}{9}\tau r_e \rho \text{ and } \text{IWP} = \frac{\tau^{\frac{1}{0.84}}}{0.065} \tag{3}$$

Here, ρ is the density of liquid water. IWP was derived from aircraft observations conducted by Heymsfield (2003) in 13 midlatitude and 6 tropical ice clouds.

DCOMP runs a forward model which relies on look up tables (LUTs) of several pre-computed radiative properties, such as cloud transmission, cloud reflectance, cloud emissivity and cloud spherical albedo. Though the use of LUTs increases the error due to interpolation, the computational time is significantly less than continuous RTM calculations. The LUTs are composed of: 45 bins for sensor and solar zenith angle between 0 and 88 degrees; 45 bins for relative azimuth distance between 0 and 180; 29 τ entries from -0.6 to 2.2 on a log10 scale; and 9 r_e entries from 0.4 to 2.0 on a log10 scale.

The radiative transfer equations used by the forward model will be discussed in detail later but, for now, we present a review of the upstream requirements needed. Several variables, such as outgoing cloud transmission and cloud reflectance, are calculated using a radiative transfer model by assuming a plane-parallel, homogeneous cloud. This assumption is robust, but only for fully cloudy pixels. To identify these, DCOMP takes input from the ABI Cloud Mask Algorithm (CM) (Heidinger, 2010). The ABI CM is a multispectral retrieval. DCOMP processes pixels flagged as "probably cloudy" or "cloudy" by the CM.

The second upstream requirement is information on cloud phase. Ice and water have different spectral signatures in the NIR, so different look-up tables are generated. This decision is made on a pixel-by-pixel basis using input from the PATMOS-x Cloud Type (CT) algorithm (Pavolonis, 2005). The CT algorithm uses brightness temperature (BT) thresholds of the 11 μm channel to categorize cloudy pixels into one of three types: Ice, Mixed, or Water. Further distinctions are made using the VIS and 3.75 μm NIR channels, but DCOMP processes all water types (including supercooled liquid water) and mixed types as water pixels and all ice types as ice pixels.

A third upstream requirement is cloud height, which is used to derive cloud transmittance (t_c) from the equation for cloud radiance (I_{toc}):

$$I_{toc} = \varepsilon_c B_c(T_c) + t_c(I_{clr} - I_a(H)) \quad (4)$$

Where ε_c is cloud emissivity, $B_c(T_c)$ is radiance for a cloud of temperature,T_c, I_{clr} is the clear sky radiance and $I_a(H)$ is the radiance contribution from the layers above a cloud of height H. Of these variables, t_c and ε_c are unknown, H and T_c, are received from the ABI Cloud Height (CH) Algorithm (Heidinger, 2010). The other variables are calculated using

the Pressure-Layer Fast Algorithm for Atmospheric Transmittance (PFAAST) radiative transfer model (RTM). The ε_c is determined during the optimal estimation process.

The fourth a priori is the modified Gamma-Hansen drop size distribution (Hansen and Pollack, 1970) which is assumed for the purpose of making the RTM calculations.

$$n(r) \propto r^{\frac{1-3v_{eff}}{v_{eff}}} \exp\left(\frac{-r}{r_e v_{eff}}\right) \tag{5}$$

The range of the distribution is limited to r from 0 μm to 80 μm and the dispersion (v_{eff}) about the effective radius is 0.1. In the case of an ice phase cloud, a distribution of habits is used, as prescribed by Baum et al. (2005). This includes droxels, plates, columns, aggregates and other varieties.

An iterative optimal estimation process (Rodgers, 2000) is used to solve for τ and r_e from the equation for top of cloud reflectance (R_{toc}). R_{toc} has a cloud reflectance component, a surface contribution and a terrestrial contribution.

$$R_{toc} = R_c(\tau, r_e) + \frac{A t_{c,0}(\tau, r_e) t_c(\tau, r_e)}{1 - AS(\tau, r_e)} + R_{e,toc}(\tau, r_e) \tag{6}$$

Where R_c is cloud reflectance, A is surface albedo, $t_{c,0}(\tau, r_e)$ is incoming cloud transmittance, $t_c(\tau, r_e)$ is outgoing cloud transmittance, as seen earlier, and $S(\tau, r_e)$ is spherical cloud albedo. A is assumed to be a Lambertian surface and R_c, $t_{c,0}$, and S are taken from the LUTs. $R_{e,toc}$ is the terrestrial emission, which is negligible for the 1.6 μm and 2.2 μm channels, but non-negligible for the 3.75 μm channel, which we are using here. This factor has to be modified slightly so that the units are the same as the reflectance terms.

$$R_{e,toc} = \frac{\pi d^2}{\mu_0 F_0} I_{toc} \tag{7}$$

Where μ_0 is the cosine of the solar zenith angle, θ_0, F_0 is the solar constant and d is the Earth-Sun distance.

R_{toc} is what the satellite would see if there were no atmosphere above the cloud, which is not realistic. An atmospheric correction must be performed to account for the effect of the atmosphere above and below the cloud.

$$\mathrm{R_{toc}} = \frac{R_{toa} - R_{sc}}{t_a(\theta_0, \theta)} \tag{8}$$

Where R_{toa} is the satellite observed top of atmosphere reflectance, R_{sc} is the single scattering component from the layers of atmosphere above the cloud and t_a is the two way atmospheric transmission above the cloud. θ_0 and θ are incoming and outgoing zenith angles, respectively.

Accounting for the transmission through the layer below the cloud is accomplished by modifying the assumed surface albedo.

$$A_v = At_b(\theta_0, \theta) \tag{9}$$

Where A_v is the virtual surface albedo and t_b is the two way transmission through this layer. This leads us to the final radiative equation, which is solved for τ and r_e in the iterative optimal estimation (OE) process.

$$R_{toc} = R_c(\tau, r_e) + \frac{A_v t_{c,0}(\tau, r_e) t_c(\tau, r_e)}{1 - A_v S(\tau, r_e)} + R_{e,toc}(\tau, r_e) \tag{10}$$

The OE compares a measurement matrix, **y,** to a first-guess reflectance F(**x**, **b**), where **x** is a first guess a priori state vector and **b** is the forward model parameter vector.

$$F(\boldsymbol{x}, \boldsymbol{b}) = R_c(\boldsymbol{x}) + \frac{A_v T_0(\boldsymbol{x}) T(\boldsymbol{x})}{1 - A_v S(\boldsymbol{x})} + R_e(\boldsymbol{x}) \tag{11}$$

This is used to establish a cost matrix *J*.

$$J = \left(\mathbf{y} - \mathbf{F}(\mathbf{x}, \mathbf{b})\right)^{\mathrm{T}} \mathbf{S_y^{-1}} \left(\mathbf{y} - \mathbf{F}(\mathbf{x}, \mathbf{b})\right) + (\mathbf{x_a} - \mathbf{x})^{\mathrm{T}} \mathbf{S_a^{-1}} (\mathbf{x_a} - \mathbf{x}) \quad (12)$$

Where the difference between the observation and the first guess is weighted by the uncertainty covariance matrix, $\boldsymbol{S_y^{-1}}$. The difference between the a priori, $\mathbf{x_a}$, and the state vector, $\mathbf{x}$, which will become the returned vector, is weighted by the uncertainty covariance matrix $\boldsymbol{S_a^{-1}}$. $\mathbf{x}$ is varied during the retrieval process until J is minimized. The final $\mathbf{x}$ is the returned τ and r_e retrieval.

This algorithm was applied to GOES-12 imager data (Menzel and Purdom, 1994). The methodology of identifying small particle regions in the retrieval and verifying their collocation with strong updrafts is described in section 3.

III. Methodology

A. Data

The phenomena of interest are small compact regions where the effective radius is significantly smaller than that of the surrounding anvil. These regions will be referred to as "Small Particle Signatures" (SPS). This terminology is both descriptive and reflective of the potential relationship between the formation of these regions and the dynamic properties of the storm in which they occur. During the process of selecting the SPS, which is discussed in the following section, the primary filter used was GOES-12 10.7 μm brightness temperature. Only SPS in the coldest region of a convective anvil were considered as cases.

The SPS identified in this study are based on effective radius (r_e) retrieved by DCOMP applied to GOES-12 imager data. It was determined that, for the majority of the study area, the most useful range of r_e was from 15 μm to 30 μm. We were not concerned about variations in particle size greater than 30 μm, so that was deemed an appropriate upper limit.

30 dBZ NEXRAD Echo Top Height (ETH) data is used in validation. It has been established that the presence of a 30-dBZ echo above the freezing level (8 – 9km in the US Standard Atmosphere, 1976) is associated with greater ice concentrations and heavier precipitation (Zipser, 1994; DeMott and Rutledge, 1998). ETH data was down-sampled to match the satellite dataset (0.04 degrees), while preserving the maxima.

The region of interest was over the US Great Plains and Midwest, due to the prevalence of strong convection in that region. The area boundaries are defined by longitudes -84.0 W to -103.5 W and, latitudes 28.0 N to 46.0 N.

We chose four convective days: April 25, 2008, May 10, 2008, May 22, 2008 and May 8, 2009. The criteria for the selection was based on these days having a qualitatively large number of hail and tornado reports within the study area, according to the Storm Prediction Center archive of storm reports (Storm Prediction Center). For example, May 22, 2008 had 48 tornado reports and 144 hail reports, 12 of which were large hail (> 2" in diameter).

Given the large size of our study area it was subdivided into four regions (Figure 7). These regions are not uniform as they were dictated by the storm tracks to minimize errors, such as double counting due to a track moving from one region to the other. Though all four days have significant convection, the storms are not uniformly spread throughout the study area. On any given day, one or two regions may have no convection at all, while the other regions show the majority of the activity.

Figure 7: The study area, divided into 4 sub-regions. (Google Earth)

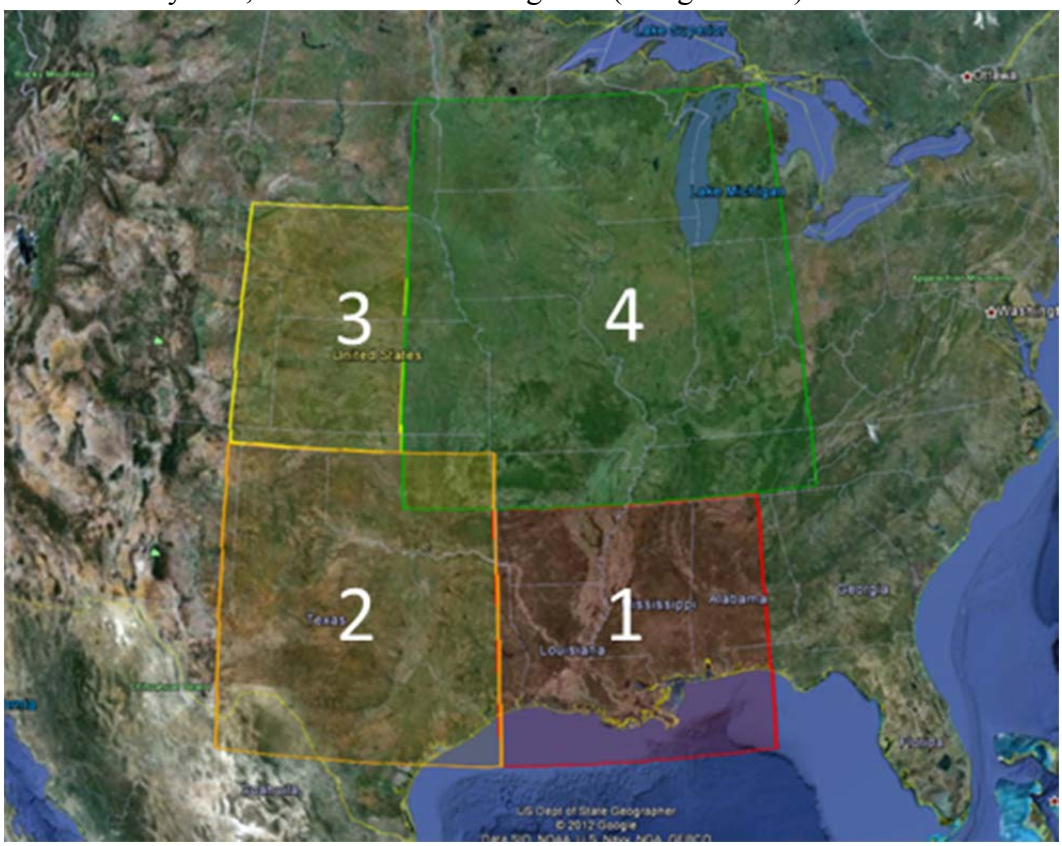

B. Manual Identification of Small Particle Signatures

Based on the hypothesis that the SPS are associated with the most active region of the storm, it was appropriate to utilize overshooting top research for guidance on where updraft-associated SPS were likely to occur. The seminal work on identifying overshooting tops in IR satellite imagery was done by Bedka, et al. (2010). The requirements for the automated overshooting top detection were: 1) the anvil was 225 K or less and 2) the overshooting top region was 215 K or less. Using these constraints as a guide, potential SPS were only added if they occurred in regions where the 10.7 μm brightness temperature was less than 215 K (Figures 8 and 9).

Figure 8: An example of the comparison between 10.7 μm Brightness Temperatures and a DCOMP effective radius retrieval showing how small particle signatures were selected from within the regions colder than 215 K. Not all areas which appear to match the criteria for SPSs occurred in the coldest regions and they were not selected. Two regions are highlighted in this convective cluster from May 22, 2008.

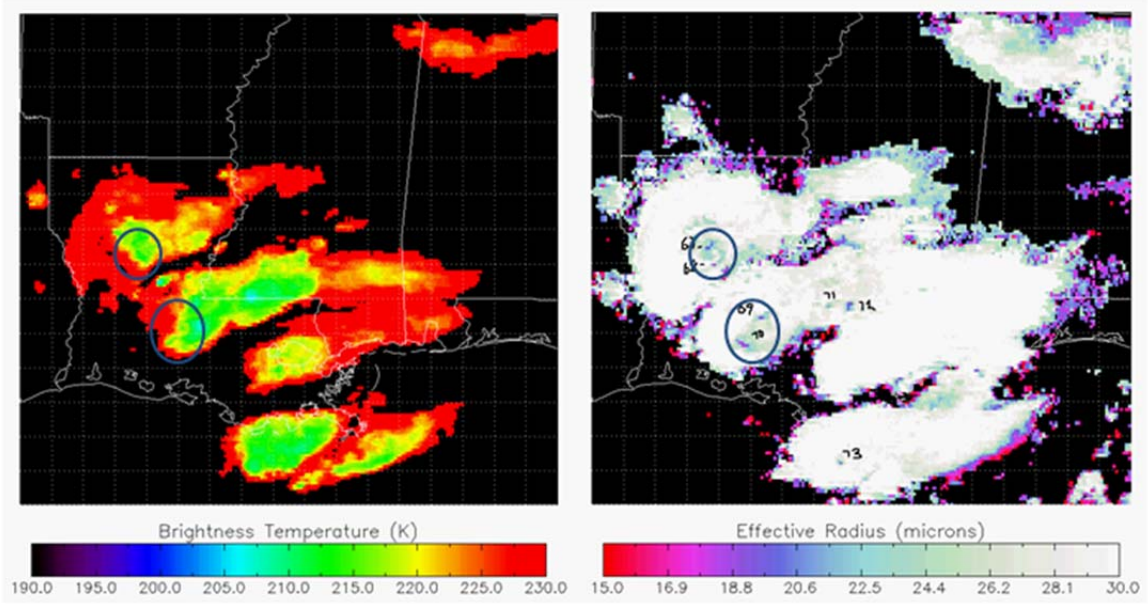

Figure 9: In this example, regions that look like SPSs, but are not associated with cloud tops less than 215 K are highlighted.

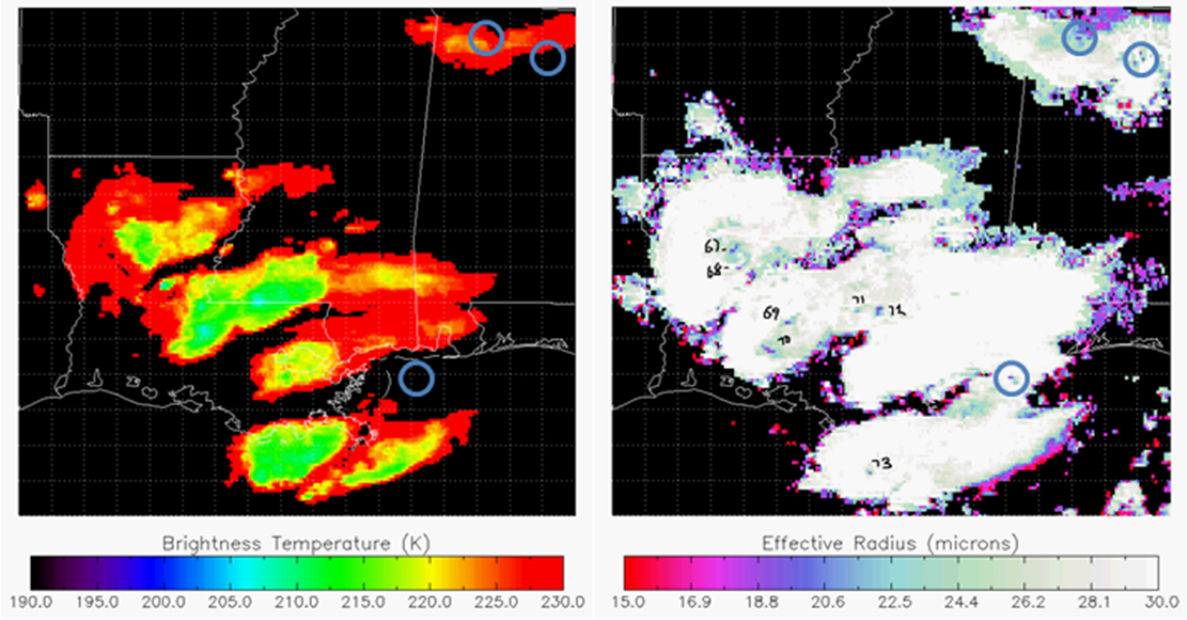

SPS are very non-uniform, which made automatic detection impractical for this study, as such all SPS identification was performed subjectively. No constraints were put on the shape of the SPS, but the region was required to be at least two pixels in size. The vast majority of the small particle signatures for these mid-latitude storms had an effective radius of 20 μm or less and an anvil effective radius of 24 μm – 30 μm or greater.

This criterion resulted in the identification of 343 SPS occurrences over the four days and four regions. SPS occurred in a variety of convective scenarios such as, linear, complex and discrete convection (Table 2).

Table 2: The distribution of SPS by day and region.

	Region 1, South East	Region 2, South West	Region 3, North West	Region 4, North East	Totals
April 25, 2008	4	61	0	8	73
May 10, 2008	0	0	0	16	16
May 22, 2008	165	10	40	0	215
May 8, 2008	0	0	0	39	39
Totals	169	71	40	63	**343**

C. Validating Small Particle Signatures

Once SPS were identified, the 30 dBZ ETH was used to verify collocation with radar-inferred updrafts. Due to the coarse resolution of both data sets and the possibility of parallax errors, SPS within 0.2 degrees, in any direction, of a 30 dBZ ETH inferred updraft were considered associated with that updraft. Over CONUS, this is between 15 and 19 km in the E-W direction and 22 km in the N-S direction. The time resolution is 5 minutes for the radar data and typically 5 – 17 minutes for the GOES DCOMP output.

According to the Standard Mid-latitude Summer Atmosphere, the tropopause is typically located between 13 and 17 km (Figure 10). The 30 dBZ ETH does not indicate the

cloud height, but rather the height of a significant echo region, therefore a 30 dBZ echo near the tropopause would suggest a cloud top which is higher, allowing us to infer a strong updraft. For our validation analysis, 10 km is used as the minimum 30 dBZ echo height which would be considered significant. For example: An SPS collocated with a 14 km echo would be recorded as incident with a strong updraft, but an SPS collocated with an 8 km echo would not.

Figure 10: The Standard Mid-latitude Summer Atmosphere. (Naval Research Laboratory, Standard Atmosphere).

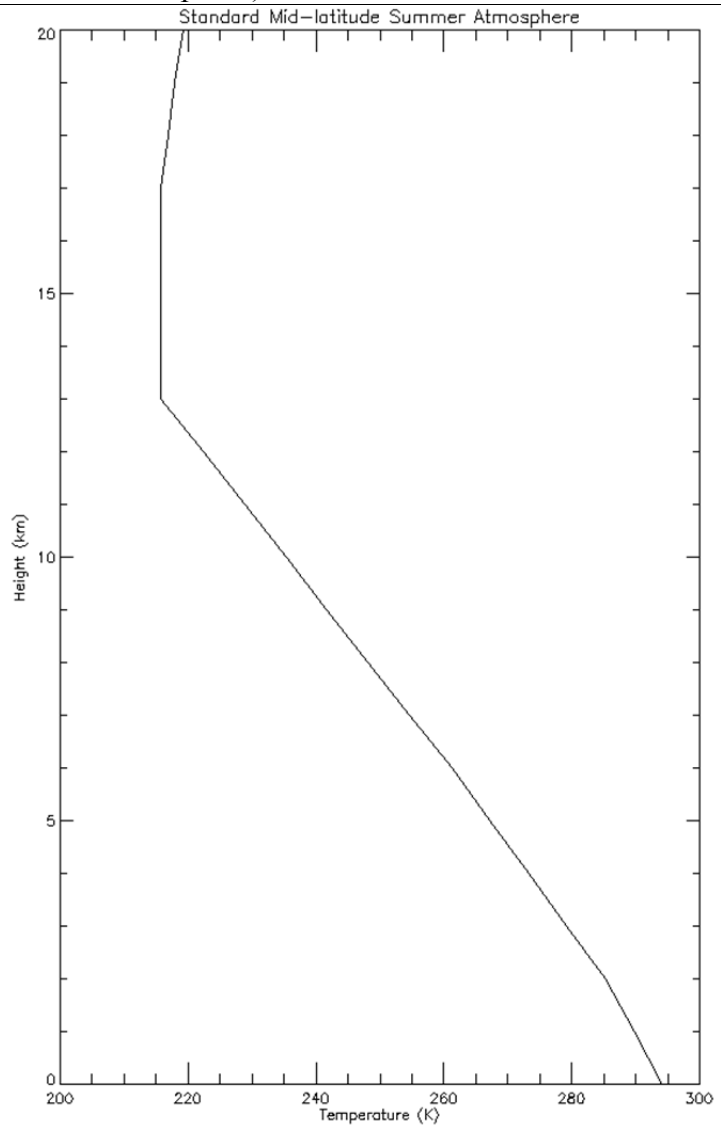

D. Identification of Initial SPS

During the lifetime of a storm, one updraft may produce many SPS. The final step in the analysis process was to determine which SPS were the first produced by a given updraft. These initial SPS were used to examine the relationship between an increase in the strength of an updraft, inferred from an increase in 30 dBZ ETH, and the production of the first SPS.

This required two parameters: the largest positive change in ETH and the time between the endpoint of that change and the appearance of the first SPS associated with that updraft. This time parameter is called the lag. Lag is negative if the SPS occurred after the endpoint and positive if it occurred before. Figure 11 shows a time series from April 25, 2008 where these two parameters are identified.

Figure 11: This example of an updraft from April 25, 2008 shows a clear "largest positive change" in ETH, +2 km between 2055 UTC and 2100 UTC (red bracket). The first SPS associated with this updraft occurs at 2115 UTC, a 15 minute lag (although it should be noted the GOES-12 imager has a 30-minute gap between 2045 and 2115 UTC, so the actual lag may have been less). The red dots indicate the time when an SPS was observed.

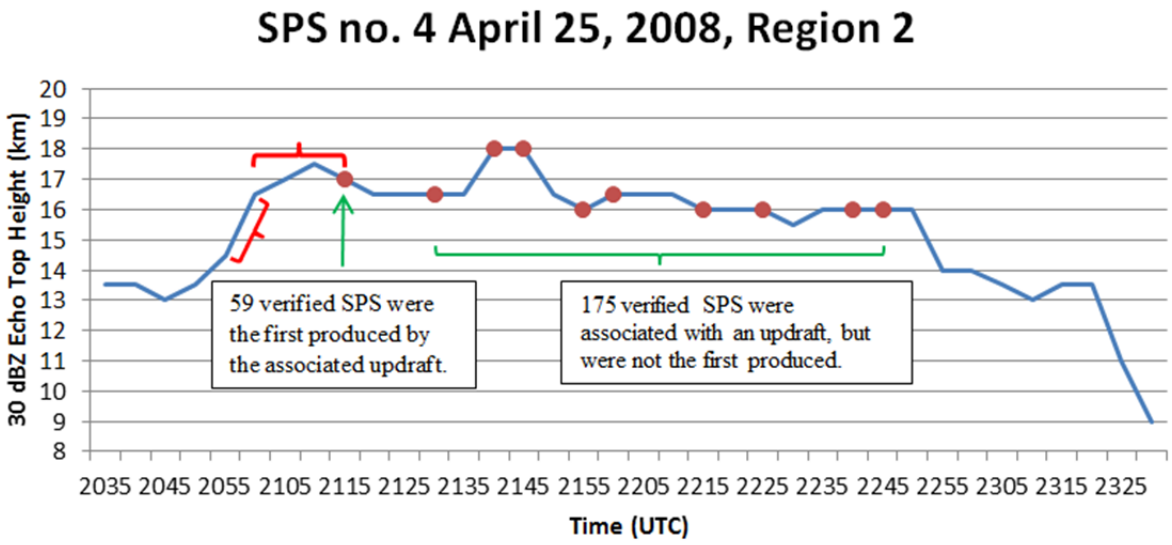

At this point, it is necessary to address the introduction of error due to ambiguity in the data sets and subjectivity of the manual analysis. As shown in Figure 12, an updraft from

May 22, 2008 produced an SPS 5 minutes after a 2.5 km increase in Echo Top Height, but before a subsequent 3 km ETH increase. It is likely that the 2.5 km increase of 30 dBZ ETH was correlated to this SPS just as much as the 3 km increase, so a 0 minute lag could have been attributed. However, for consistency the *largest* positive change is the controlling parameter, as such, this SPS was attributed a lag of +15 minutes.

Figure 12: This is an example of an ambiguous relationship between the largest positive change and the first SPS. The first SPS is most likely the result of the 2.5 km growth in ETH from 2108 UTC to 2113 UTC, but in the interest of consistency, it was attributed to the 3 km growth from 2118 UTC to 2123 UTC. The red dots indicate the time when an SPS was observed.

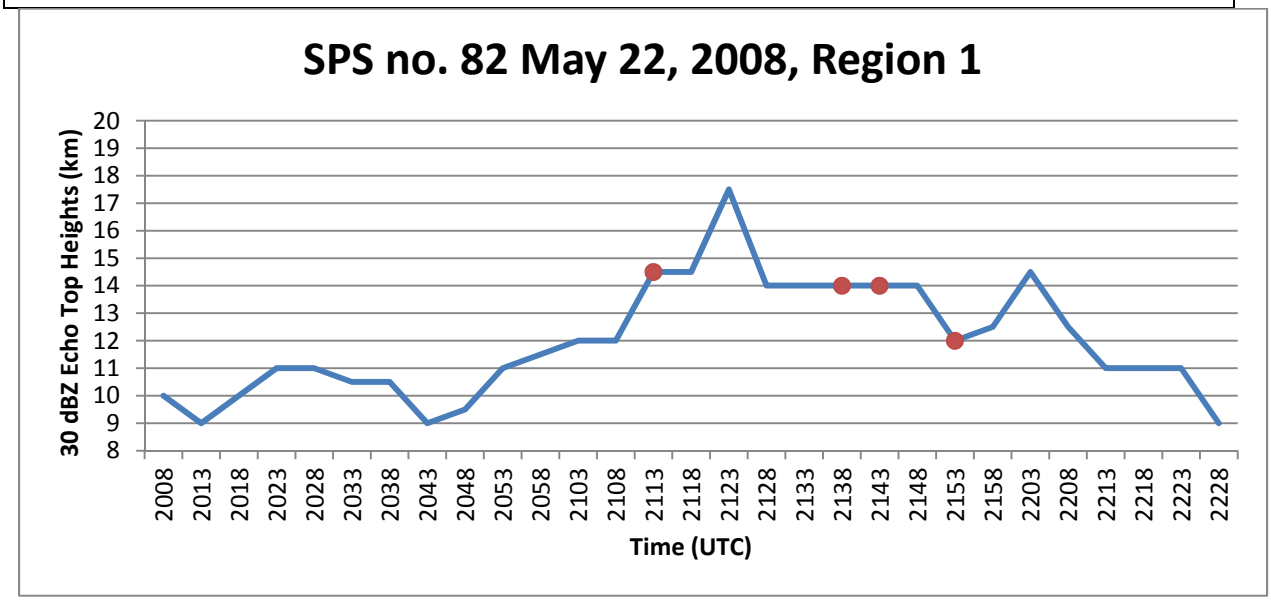

IV. Results and Analysis

The results fall in to two categories: rate of incidence, which establishes the frequency with which small particle signatures occur coincident with strong updrafts, and lag, which describes the relationship between the growth of an updraft and the first appearance of SPS.

A. Rate of Incidence

In total, 343 SPS were identified. For the full dataset, 68.2% of SPS were associated with strong updrafts. The highest rate of collocation was 93.8% (15 of 16 SPS were collocated), on May 10, 2008 in Region 4. The lowest rate was 61.5% (24 of 39 SPS) on May 8, 2009 region 4. Both of these are small sample sizes, but looking at the largest single-region sample, Region 1 from May 22, 2008, 113 of 165 SPS were incident with strong updrafts (68.5%). The second largest sample, from Region 2 on April 25, 2008, had 40 of 61 SPS incident with updrafts (65.6%). This suggests that, as the sample size increases, the rate of incidence converges to the full dataset result. The complete results are summarized in Table 3.

Table 3: The full results for the rate of incidence analysis.

Date	Region	#SPS	Incident w/Updraft	Percent
2008-04-25	1	4	3	75.0
	2	61	40	65.6
	4	8	6	75.0
2008-05-10	4	16	15	93.8
2008-05-22	1	165	113	68.5
	2	10	7	70.0
	3	40	26	65.0
2009-05-08	4	39	24	61.5
	Totals	**343**	**234**	**68.2**

In Figure 13, tornado, hail and wind reports from May 22, 2008 are plotted on a Google Earth image of the four regions. The reports are concentrated in Region 1, where there was a massive MCS, and Region 3, where severe convection developed along a warm front. In Region 2, a discrete cell late in the time period produced a small number of reports and Region 4 has no reports. Region 1 and 3 produced the most SPS, with a handful being produced by the severe storm in Region 2. By contrast, Region 4 had no SPS, in spite of

having some non-severe convection over Iowa, Missouri and Illinois. Though a different type of study would be necessary to establish a connection between SPS production and severe weather, this example shows that SPS are more commonly associated with potentially severe convection.

Figure 13: The distribution of storm reports from May 22, 2008. The storm reports outside of the study area are not included in the analysis.

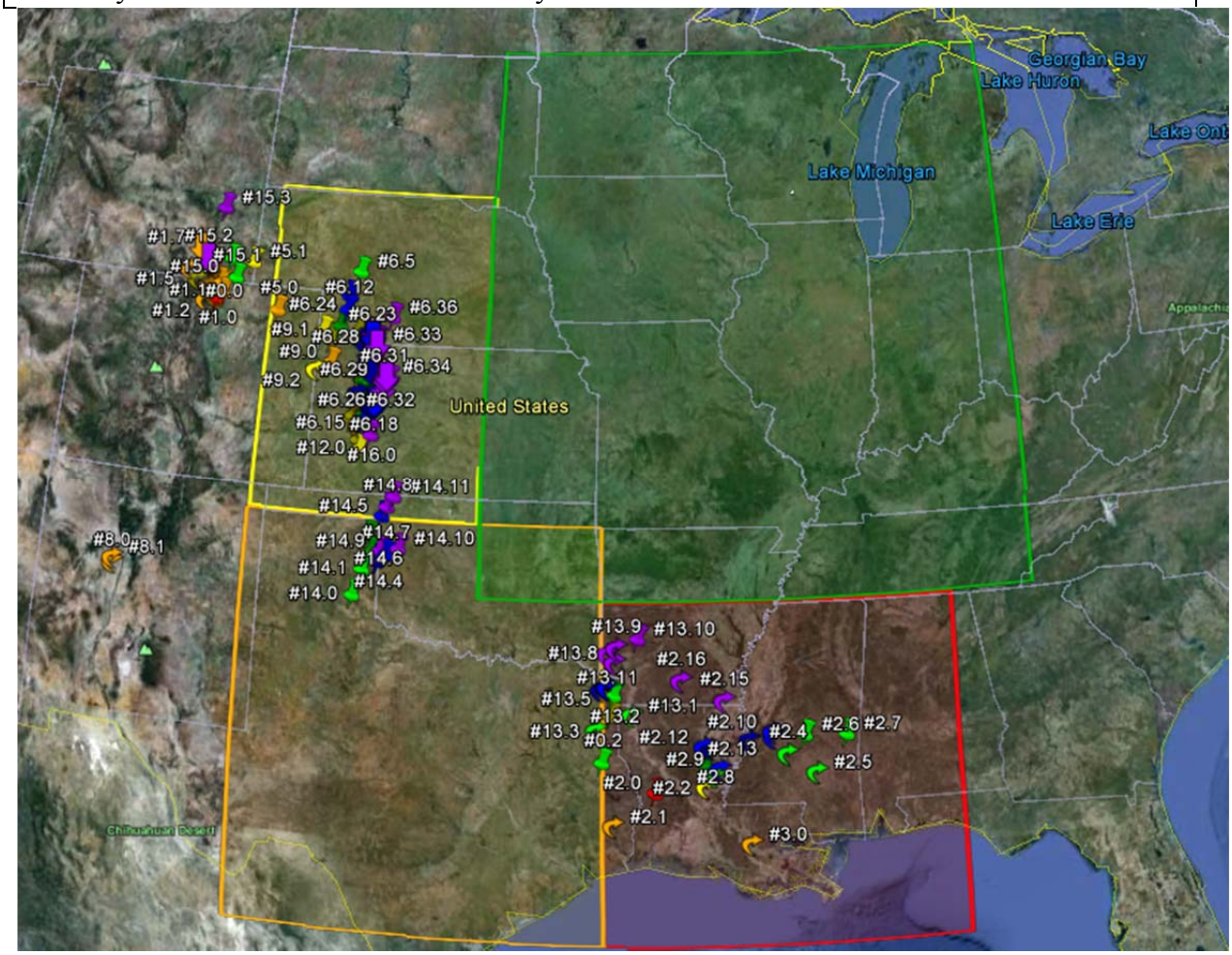

The 31.8% of SPS which were manually identified based on their collocation with the coldest region of the anvil, but were not collocated with a strong updraft fall roughly into 3 categories. The first is an SPS located on a sharp gradient between the coldest temperatures

and the warmer clouds near the anvil edge, like on April 25, 2008 (Figure 14). Given strong updrafts often occur near these brightness temperature gradients, this example shows the ambiguity in manually identifying an SPS possibly associated with an updraft versus benign thinning of cirrus anvil. The second is, based on our analysis, very rare, but occurred on May 22, 2008 (Figure 15). In this example, a high, cold anvil cast a deep shadow over a lower stratus cloud. In the r_e field, the two clouds are indistinguishable, so this region was identified as an SPS. It is actually a false detection caused by the shadow. This SPS also occurred in a region with a strong BT gradient, further complicating the identification. The third category is of SPS which were not located close enough to a 30 dBZ ETH updraft to verify. From the same time on May 22, 2008, we can see a dense cluster of SPS, three of which verified and one which did not (Figure 16).

Figure 14: This is an example of an SPS which was identified, but was not collocated with an updraft (far western Arkansas). It was selected because it is fully surrounded by larger r_e and is on or near the coldest temperatures of the anvil. This scene is from April 25, 2008.

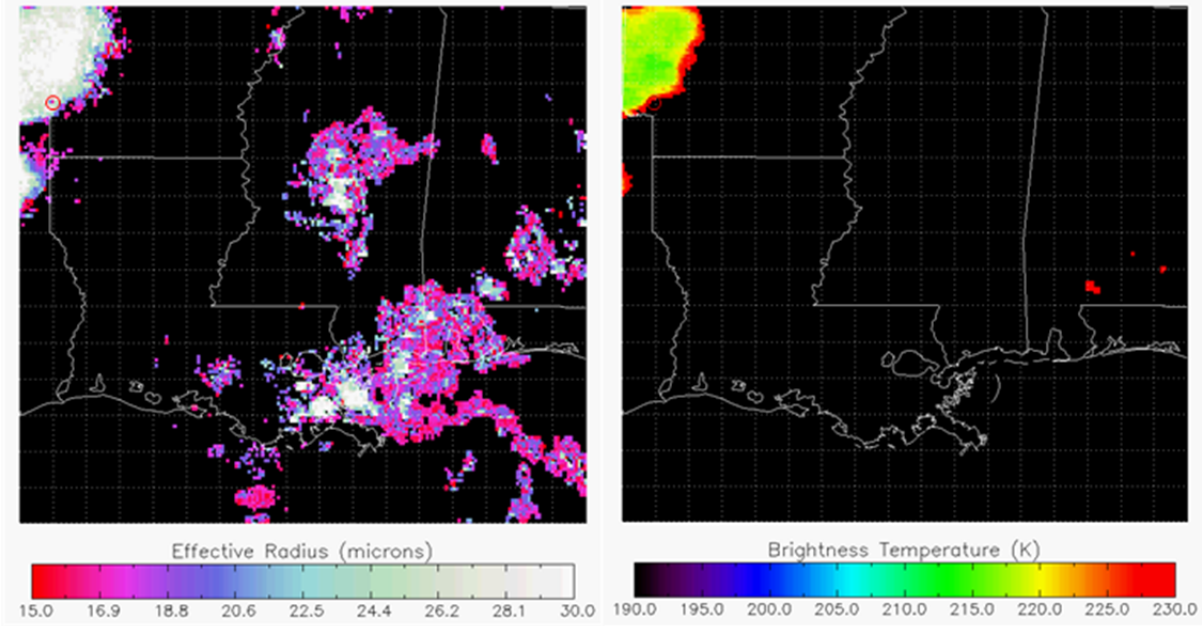

Figure 15: This identified SPS is actually an incorrect identification, caused by the shadow of a large anvil over lower stratus clouds.

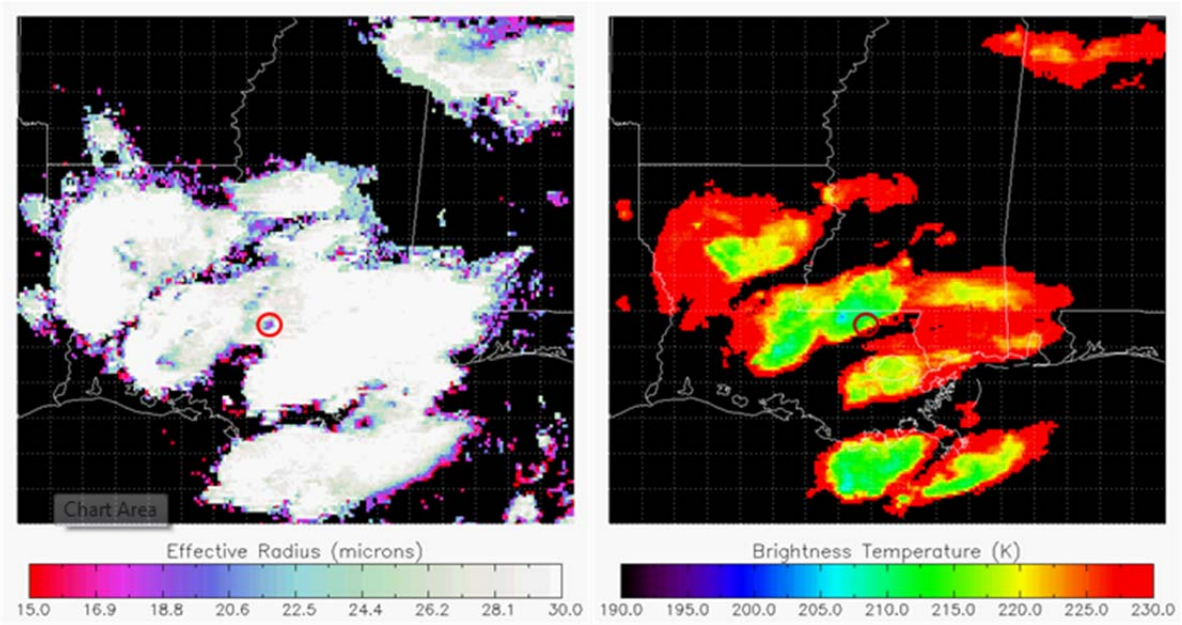

Figure 16: Four SPS were identified in this cluster, but the northern most did not verify.

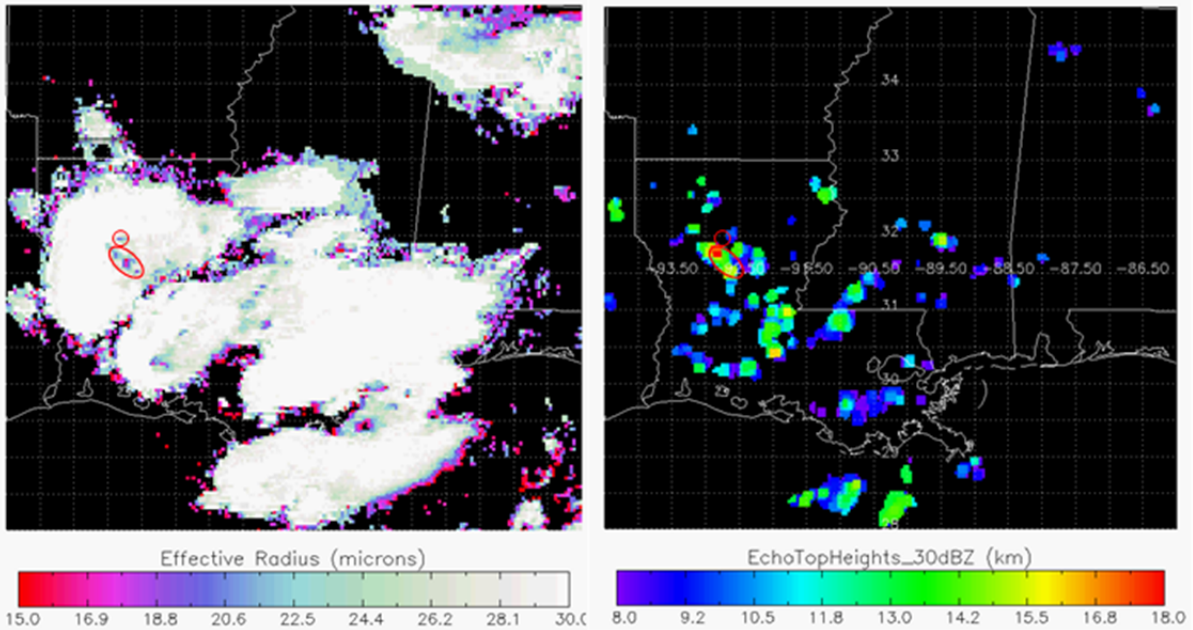

B. Lag Analysis

A single updraft can produce multiple SPS during its life. The lag analysis was designed to investigate the relationship between the first SPS produced and the variation in ETH intensity. Of the 343 identified SPS, 234 verified as associated with a radar inferred updraft. Of these, 59 were the first SPS produced by their associated updraft. These became the cases for the lag analysis. In Figure 11, the ETH was plotted against Time for updraft number 4 from Region 2 on April 25, 2008, with markings at the times when an SPS was observed. The largest positive change in ETH occurred between 2055 and 2100 UTC. At 2115 UTC, SPS no. 4 was observed, giving it a lag of -15 minutes.

The results of this analysis are shown in Figure 17. The most important result is about half (50.8%) of all first SPS occurred between 5 and 30 minutes after the largest positive change in ETH. The sensitivity of satellite and radar observations to different hydrometer sizes and differing opacity of thunderstorms is the major factor in this finding. An updraft is comprised of both cloud particles and precipitation particles. The radar is sensitive to the precipitation particles and can remotely sense these precipitation-sized particles in all vertical portions of the thunderstorm. Since thick water and ice clouds are quite opaque in the VIS and IR satellite observations, these satellite observations reflect only impacts at the cloud-top. For example, the radar can detect precipitation sized hydrometeors being lofted higher within a thunderstorm sooner than the updraft will impact the cloud-top anvil. Given these fundamental differences in the remote sensing tools, it is expected that the radar signature should precede the satellite signature, by an amount of time related to the updraft speed and vertical distance between the 30 dBZ ETH and cloud-top. The relatively short lag time shown in Figure 17 is interesting because it indicates that SPS detection can be

useful as a diagnostic or nowcasting tool. In support of this interpretation, we found that 30.5% of the first SPS occurred exactly incident with the endpoint of the largest positive change. With the 50.8% lagging SPS, this accounts for 81.4% of the initial SPS.

Figure 17: The histogram of the results from the Lag analysis. 81.4% of the first SPSs occurred between 0 and 30 minutes after the endpoint of the largest positive change in 30 dBZ Echo Top Height. The 7 SPSs which lead the endpoint are attributed to human error complicated by the coarseness of the datasets. The 4 SPSs which lagged the endpoint by more than 30 minutes are attributed to missed detections, resulting in the measurment being made to the second or third SPS, due to the coarse spatial resolution of the current GOES imager.

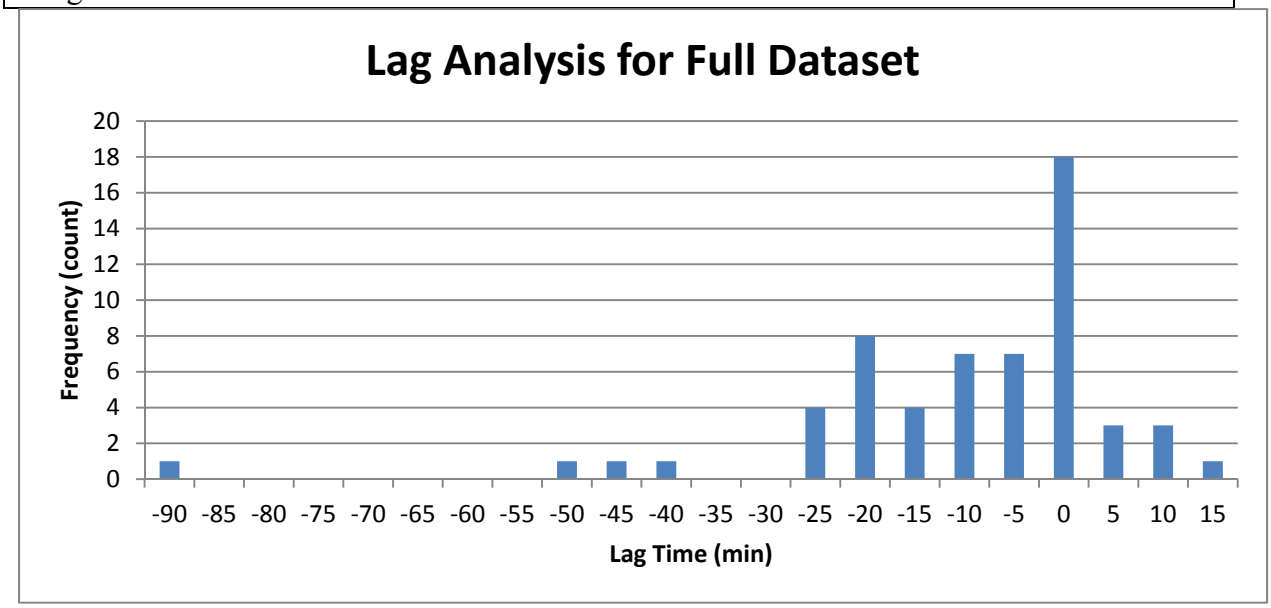

The lag analysis provides further demonstration of two sources of error in this study. The first is error due to the nature of analysis by manual inspection. The motivation for this has already been discussed in detail, but the results can be seen in the 7 SPS which occurred *before* the largest positive change in ETH. This is not reasonable, dynamically, but due to ambiguity in the spatial resolution of the radar or significant variations in updraft strength, an accurate assessment was difficult in some cases.

The other source of error is missed detections due to the coarse spatial resolution of the GOES satellite. This error manifests itself as seen in the 4 SPS which occurred more than 30 minutes after the largest positive change in ETH. In these cases the first SPS was most likely missed due to spatial resolution, resulting in the lag being computed for the second or third SPS, consequentially giving an excessive lag time. The relationship between a GOES pixel and the horizontal extent of an updraft will be discussed in the next section.

C. Introduction of error from spatial resolution

The GOES-12 satellite, which was the operational GOES-East satellite during 2008 and 2009, has a spatial resolution of 4 km at nadir (at 75 W). However, over the continental United States, the resolution varies from 4.5 km over southern Florida to as much as 8 km over the Montana/Canada border. Over most of our study area, one can assume a spatial resolution of 5 – 6 km.

In Figure 18, simulated cloud top temperature from the Wisconsin Dynamical/Microphysical Model (WISCDYMM, Wang, 2007) clearly shows the structure of an anvil, including the highlighted updraft feature. It is clear that the updraft is 10 km or less horizontally, which presents a potential challenge for detection with GOES. As we have established, SPS are associated with strong updrafts, which suggests they have a similar spatial resolution.

Figure 18: Simulated cloud top temperature from WISCDYMM. The red box is 10 km x 10 km with four 5 km by 5 km boxes inside, scaled to the image. (Courtesy of Kai-Yuan Cheng)

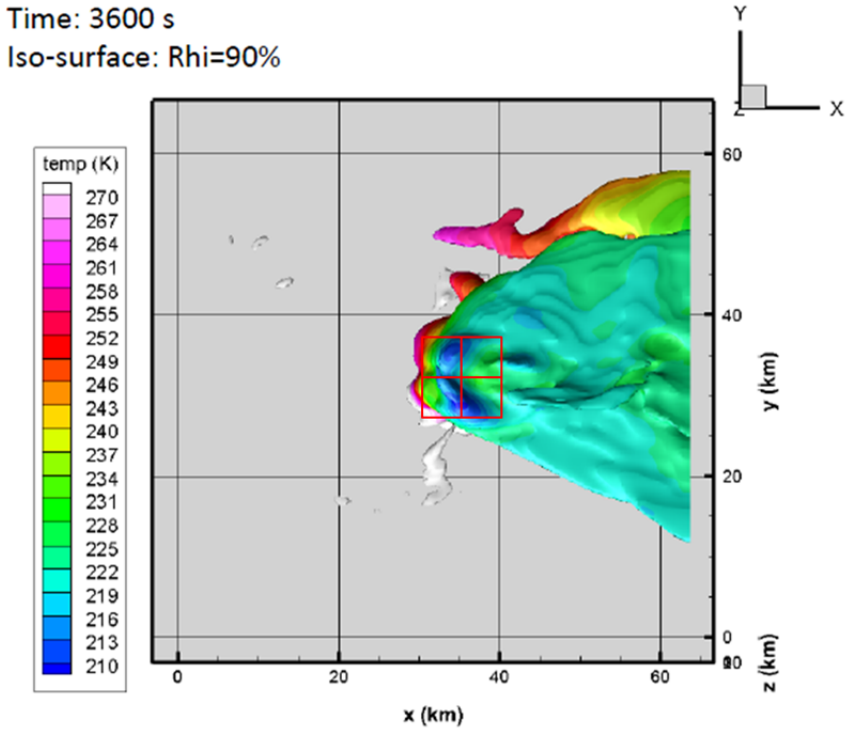

This situation could lead to missed detections, as demonstrated in Figure 19. If an SPS fully intersects one or more GOES pixels, then it will likely be detected. If the SPS only partially intersects a group of pixels, however, the SPS will be averaged out in each pixel and potentially missed. It is likely that this led to the 3 long lag times identified in the lag analysis (establishing this with certainty would require a separate study using a higher resolution imager).

Figure 19: A diagram illustrating how the spatial resolution of a GOES pixel could result in a missed detection for an updraft. On the left, this updraft is very well situated and will be detected by the retrieval. On the right, this updraft contributes very little to each of the four pixels and its effect will be averaged out in all four, resulting in a missed detection.

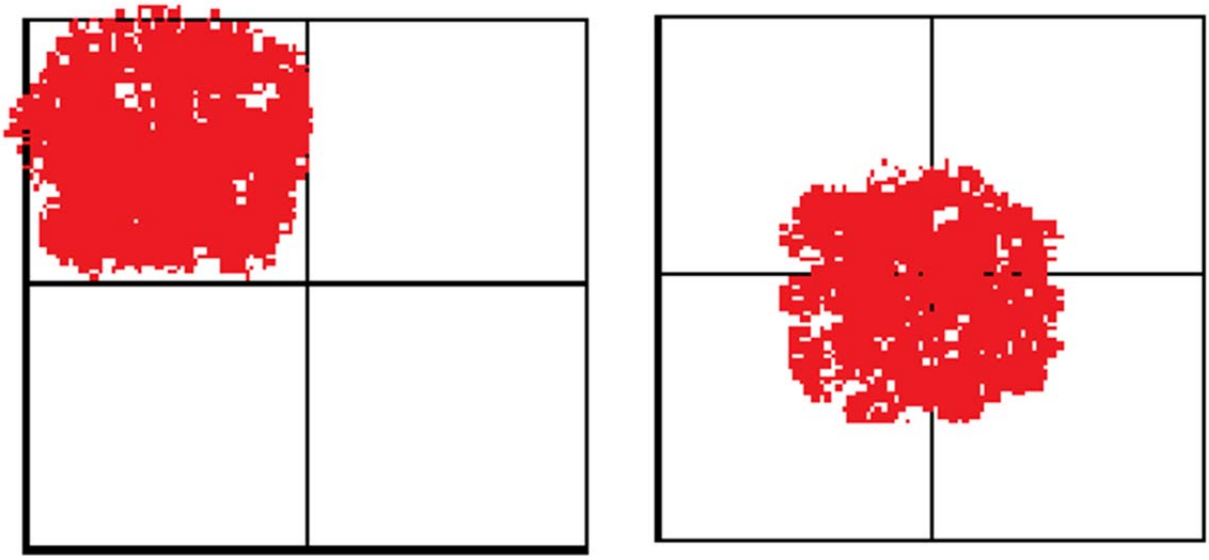

To contrast our primary data with a higher resolution sensor, we ran the DCOMP retrieval on MODIS data over a storm in Illinois on June 27, 2008. In the highlighted region in Figure 20a, a very strong and growing cell has a minimum brightness temperature of 193 K. In Figure 20b, that 195 K cloud top is associated with an SPS with an r_e of about 16 μm. In contrast, the GOES retrieval (Figure 20c) over the same storm did not detect the SPS associated with that updraft, likely due to spatial resolution. Figure 21 shows how a GOES missed detection (assuming 6 km spatial resolution) would be covered by several 1 km MODIS pixels and detected by that sensor.

Figure 20: By applying DCOMP to a MODIS image from June 27, 2008 over Illinois, the spatial resolution problem becomes clear. In a) we have the 10.7 µm brightness temperature. The cell highlighted shows cloud top temperatures around 190 K. As expected, the effective radius retrieval, b), identified a complex SPS with r_e as low as 16 µm. The DCOMP retrieval performed on GOES data over the same region (c), however, does not identify this area.

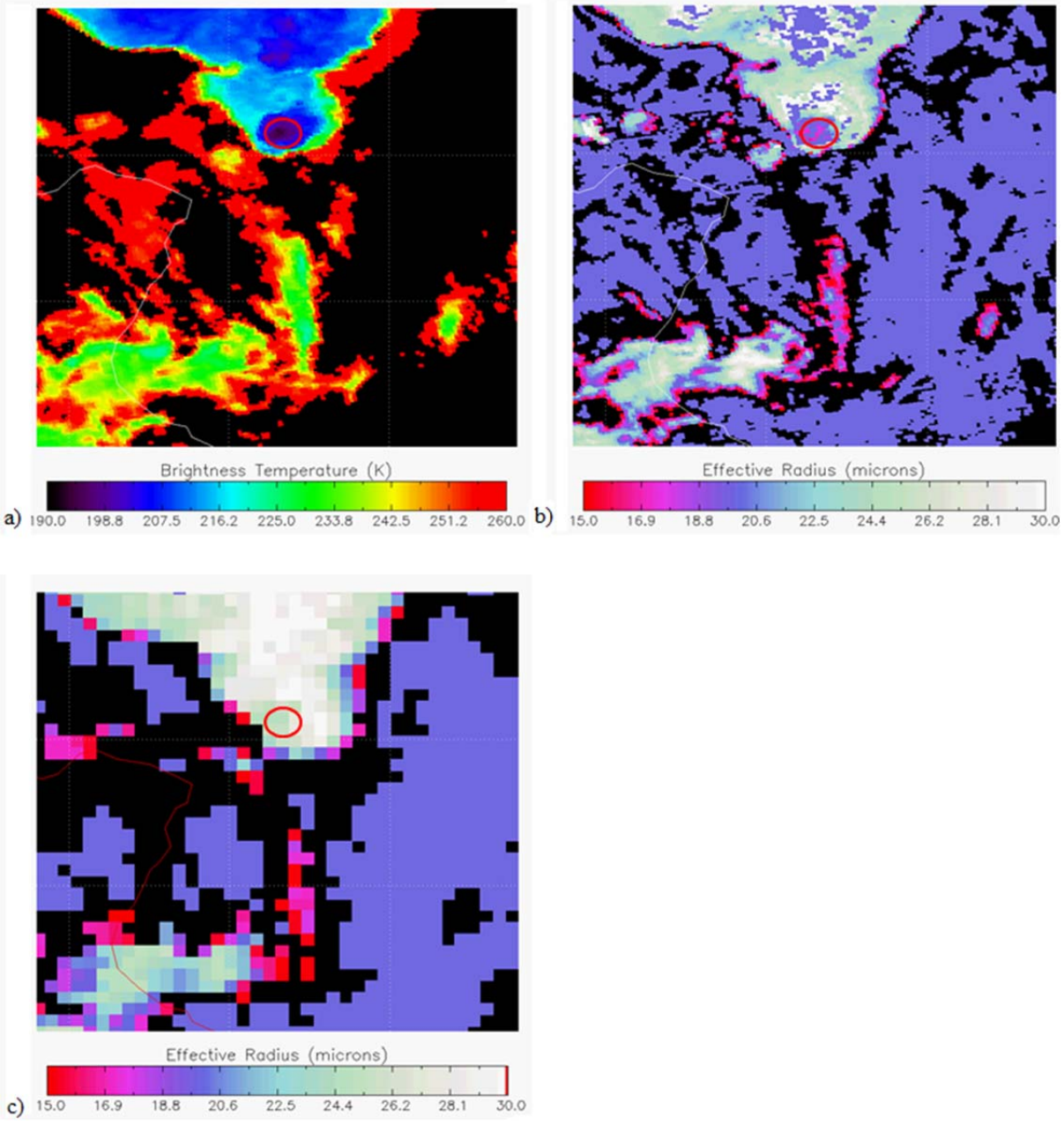

Figure 21: MODIS 1 km pixels (left) are arranged in a grid over an area covered by only 4, 6 km, GOES pixels (right). This demonstrates how a relatively large feature observed by MODIS could still be missed by poorer spatial resolution GOES.

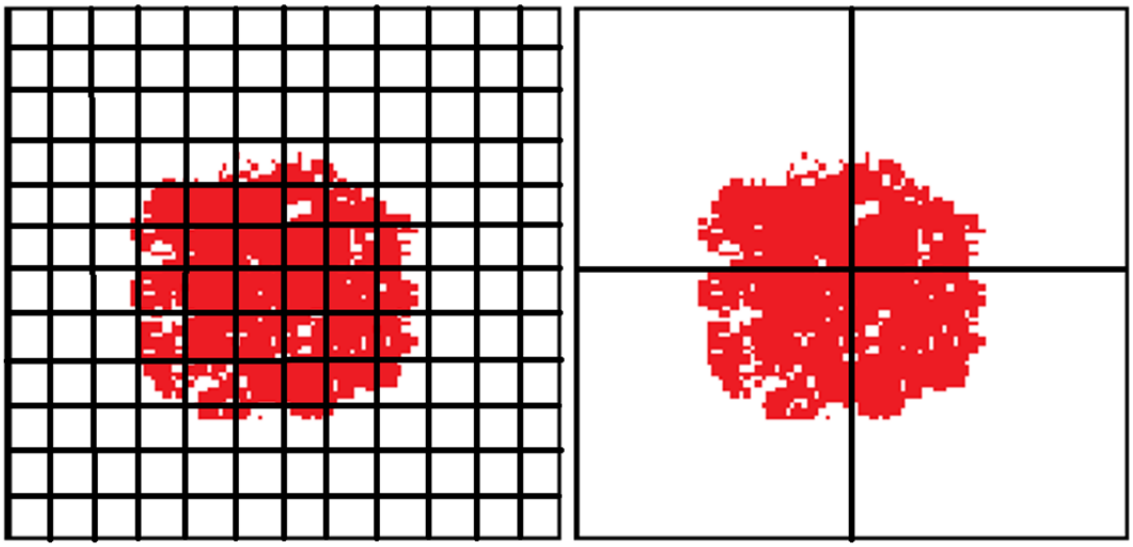

The missed detection by the GOES imager is also a result of the response of the instrument. The Northern Hemisphere is not imaged in one instant, like with a camera shutter, but is collected along the first line of pixels, then the second, etc. This introduces a slight time offset that must be taken into account in the final output and also influences the amount that neighbor pixels contribute to the target pixel. Though the majority of the total signal comes from pixel N, some of the signal is contributed from N-1 and N-2 and, less but non-negligible, from N+1 and N+2. Similarly, due to diffraction, the 8 pixels surrounding pixel N contribute a small amount to the total signal from that pixel. The result, demonstrated in Figure 22, is that a region in which MODIS observed minimum brightness temperature of 193 K was observed by GOES as 209 K. This very large discrepancy is the combined result of the course spatial resolution of GOES and the input of the surrounding

GOES pixels, which are significantly warmer than the small area around the updraft.

(Menzel, 2006)

Figure 22: The difference between the MODIS and GOES retrieved 10.7 μm brightness temperatures over the Illinois convection, June 27, 2008. On the left, we see that MODIS observed temperatures as low as 193 K near the updraft. The coldest temperature observed by GOES is 209 K. Both GOES and MODIS pixels have point spread functions which account for neighbor pixel contributions, but because so few GOES pixels cover the area of interest, the neighbor pixels exacerbate the averaging-out effect shown in Figure 21.

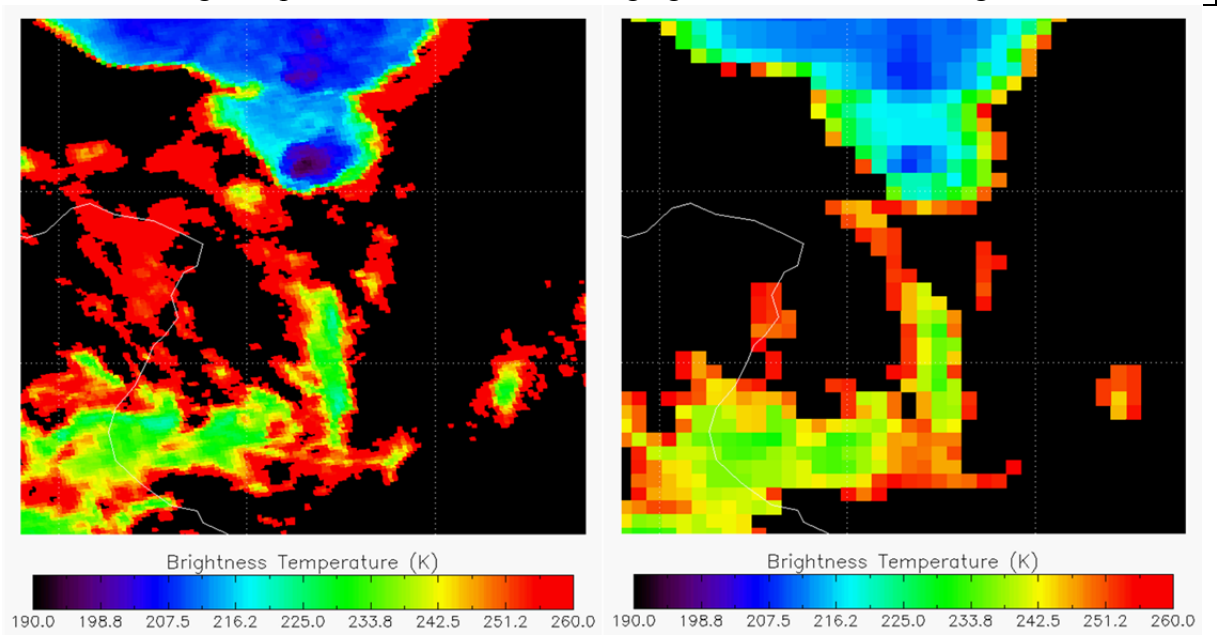

V. Conclusions

A. Summary

Previous studies have indicated that the 3.9 μm reflectance can be used to retrieve effective radius from satellite observations (Nakajima and King, 1990; Lindsey , et al., 2006). Lindsey, et al., 2006 and Lindsey and Grasso, 2008 utilized the relationship between 3.9 μm reflectance and effective radius to characterize the geographic distribution of reflectance in convective scenes over CONUS.

The Daytime Cloud Optical Microphysical Properties retrieval (DCOMP) uses look up tables generated from a forward model and an optimal estimation process to retrieve effective radius operationally from geostationary and low-earth orbiting imagers (Walther, et al., 2012). This project used DCOMP applied to GOES-12 data to study the relationship between regions in convective anvils, associated with convective updraft cores, where the effective radius is significantly smaller than the surrounding anvil.

Small particle signatures (SPS) are defined as regions of at least two pixels where the effective radius is generally 20 μm or less, and nearby anvil effective radius retrievals are 24 μm – 30 μm or greater, and are located in the coldest (<= 215 K) region of the anvil, as identified by GOES-12 10.7 μm brightness temperature. 343 SPS were manually identified. Validation was performed by comparing SPS to 30 dBZ Echo Top Height (ETH) data. An SPS was considered collocated with an updraft if it occurred within 0.2 degrees (~20 km) of an updraft core with a 30 dBZ ETH of 10 km or greater.

68.2% of the identified SPS verified as collocated with a strong updraft core. The verified SPS were distributed in all four regions of the study area and on all four days. Most of the SPS which did not verify were located near strong gradients in BT, which implied possible error in the manual identification. Other non-verified SPS were close, but not within 0.2 degrees of an updraft region. At least one non-verified SPS was a false retrieval caused by a deep shadow from an anvil on a lower stratus deck.

During the life cycle of an updraft, it may produce more than one SPS. A second analysis was performed comparing the appearance of the first SPS associated with an updraft to the growth of that updraft, inferred from the largest positive change in 30 dBZ ETH. 59 verified SPS were identified as being the first associated with an updraft. 81.4 % of these

occurred at the same time as the endpoint of the largest positive change, or within 30 minutes after that point.

From this analysis, we confirmed that SPS are caused by strong updrafts, as determined by 30 dBZ ETH, and occur shortly after intensification of the updraft. The errors present can be accounted for by error in the manual analysis or missed detections due to the coarse spatial resolution of the GOES satellite.

Most convection will not be viewed in daylight by a low earth orbiting instrument, like MODIS, more than once. Thus, the temporal resolution of geostationary observation is the most useful tool for identifying SPS; however, the spatial resolution likely limits operational usability of this data to regions where radar coverage is limited or non-existent. Over CONUS, radar has significantly higher spatial resolution and will continue to be the foremost tool for identifying strong convection.

Without access to radar, the identification of an SPS could be implemented to identify regions where a strong updraft has recently emerged or strengthened. This could be very useful for aviation weather monitoring over ocean areas. The final section suggests avenues of future work which would be necessary for moving these findings closer to operational usability.

B. Future Work

The first step in extending the applications of this work is to repeat this study over a region with sparse radar coverage to determine whether a similar association emerges. Validation for this type of study could be done using the IR overshooting top detection algorithm (Bedka, et al., 2010), pilot reports of turbulence in the vicinity or a combination of both. Many of these areas occur over the tropics, where storm dynamics are different from

those in mid-latitudes. This may result in a different microphysical structure within the updraft.

This leads to the second recommendation for future work, a climatological study, over the entire globe, using a high resolution sensor, like VIIRS or MODIS. Minimizing the chance of missed detections allows for credible findings about the frequency of SPS with respect to updraft strength, synoptic conditions, air quality and aerosol CCN availability, and geographic location. For example, recall that Lindsey, et al. (2006) found climatologically higher reflectance in the western Great Plains and lower reflectance over the Midwest and Eastern United States, which suggests a larger average r_e in that region. The range of r_e considered in this study was designed for storms which have SPS of 17 – 20 μm and an anvil average r_e of 30+ μm. A storm on the eastern edge of our domain, such as the cold front event from April 25, 2008, may have SPSs of 25 – 30 μm and an anvil average of 40+ μm (Figure 23). This would be consistent with the climatology, but would not be well shown by our choice of range. Regional variations like this would be identifiable in a climatological study. After the launch of the GOES-R ABI, a climatological study could also characterize the spatial offsets between ETH data and geostationary SPS observations more precisely.

Figure 23: This is an example of a cold front event on the eastern edge of the study area. Using the chosen range of r_e, only one SPS satisfied our criteria (left). If we change the range to better reflect the climatology of larger average r_e, several more potential SPSs become apparent (right).

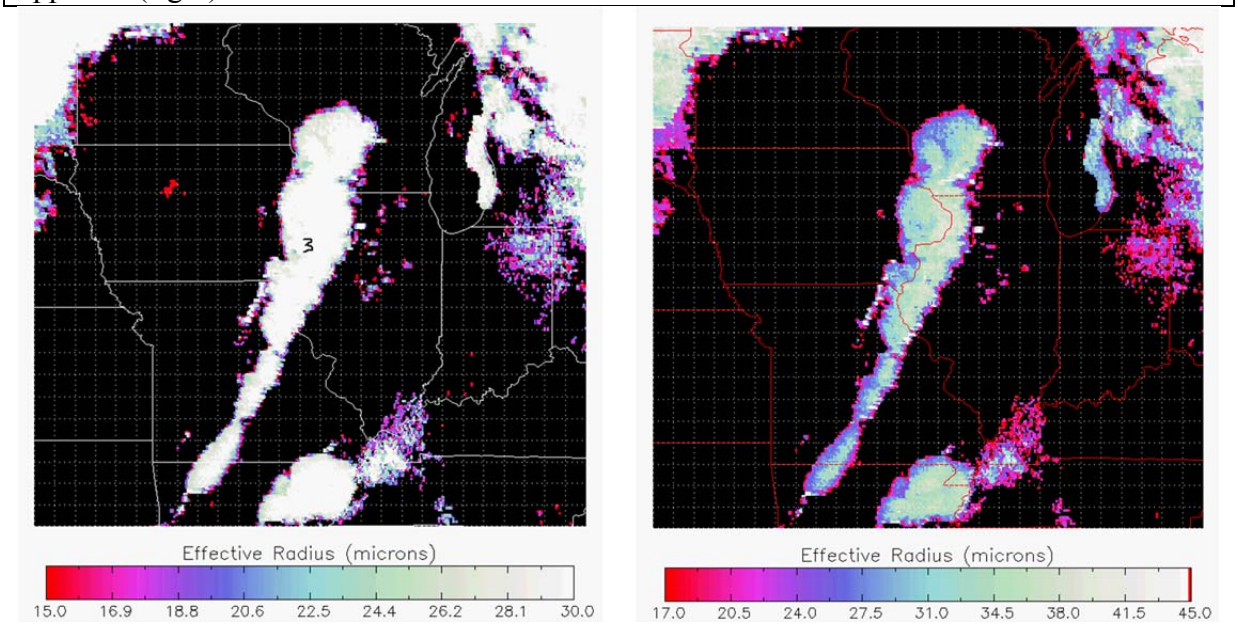

An important future avenue would be to bring this research into operational use for nowcasting and diagnosing strong convection. This would require an automated detection algorithm with a very good probability of detection. Using the cloud top temperature parameters from the overshooting top detection algorithm, candidate pixels could be narrowed down to a very small area for any storm. An iterative neighbor-checking process could be used to build a small particle signature from a single detected anomalous pixel. This would allow for SPS of varying shapes to be detected.

Works Cited

Baum, Bryan A., Andrew J. Heymsfield, Ping Yang, and Sarah T. Bedka. "Bulk Scattering Properties for the Remote Sensing of Ice Clouds. Part I: Microphysical Data and Models." *Journal of Applied Meteorology* 44.12 (2005): 1885. Print.

Bedka, Kristopher, Jason Brunner, Richard Dworak, Wayne Feltz, Jason Otkin, and Thomas Greenwald. "Objective Satellite-Based Overshooting Top Detection Using Infrared Window Channel Brightness Temperature Gradients." *Journal of Applied Meteorology and Climatology* 49.February (2010): 181-202. Print.

Bennartz, Ralf. "Global Assessment of Marine Boundary Layer Cloud Droplet Number Concentration from Satellite." *Journal of Geophysical Research* 112.D2 (2007): D02201. Print.

Bieringer, Paul, and Peter S. Ray. "A Comparison of Tornado Warning Lead Times with and without NEXRAD Doppler Radar." *Weather and Forecasting* 11.1 (1996): 47-52. Print.

DeMott, Charlotte A., and Steven A. Rutledge. "The Vertical Structure of TOGA COARE Convection. Part I: Radar Echo Distributions." *Journal of the Atmospheric Sciences* 55.17 (1998): 2730-747. Print.

Doswell, Charles A., III. "The Distinction between Large-Scale and Mesoscale Contribution to Severe Convection: A Case Study Example." *Weather and Forecasting* 2.March (1987): 3-16. Print.

Doswell, Charles A. *Severe Convective Storms*. Boston, MA: American Meteorological Society, 2001. Print.

Dworak, Richard, Kristopher Bedka, Jason Brunner, and Wayne Feltz. "Comparison between GOES-12 Overshooting-Top Detections, WSR-88D Radar Reflectivity, and Severe Storm Reports." *Weather and Forecasting* 27.3 (2012): 684-99. Print.

Edwards, Roger, and Richard L. Thompson. "Initiation of Storm A (3 May 1999) along a Possible Horizontal Convective Roll." *Preprints, 20th AMS Conference on Severe Local Storms*. Proc. of 20th AMS Conference on Severe Local Storms, Orlando, FL. Orlando: AMS, 2000. N. pag. Print.

Evans, K. Franklin. "The Spherical Harmonics Discrete Ordinate Method for Three-Dimensional Atmospheric Radiative Transfer." *Journal of the Atmospheric Sciences* 55.3 (1998): 429-46. Print.

Fulton, Richard A., Jay P. Breidenbach, Dong-Jun Seo, Dennis A. Miller, and Timothy O'Bannon. "The WSR-88D Rainfall Algorithm." *Weather and Forecasting* 13.2 (1998): 377-95. Print.

Fulton, Richard, and Gerald M. Heymsfield. "Microphysical and Radiative Characteristics of Convective Clouds during COHMEX." *Journal of Applied Meteorology and Climatology* 30 (1991): 98-116. Print.

"Glossary - NOAA's National Weather Service." *Glossary - NOAA's National Weather Service*. National Oceanographic and Atmospheric Administration, 25 June 2009. Web. 19 Nov. 2012. <http://w1.weather.gov/glossary/>.

Hansen, James E., and James B. Pollack. "Near-Infrared Light Scattering by Terrestrial Clouds." *Journal of the Atmospheric Sciences* 27.2 (1970): 265-81. Print.

Hansen, James E., and Larry D. Travis. "Light Scattering in Planetary Atmospheres." *Space Science Reviews* 16.4 (1974): 527-610. Print.

Heidinger, Andrew. *ABI Cloud Height*. ATBD. 2nd ed. N.p.: NOAA NESDIS Center for Satellite Applications and Research, 2010. Print.

Heidinger, Andrew. *ABI Cloud Mask*. ATBD. 2nd ed. N.p.: NOAA NESDIS Center for Satellite Applications and Research, 2010. Print.

Heymsfield, Andrew J., Sergey Matrosov, and Bryan Baum. "Ice Water Path–Optical Depth Relationships for Cirrus and Deep Stratiform Ice Cloud Layers." *Journal of Applied Meteorology* 42.10 (2003): 1369. Print.

Khain, A. P., D. Rosenfeld, and A. Pokrovsky. "Simulating Convective Clouds with Sustained Supercooled Liquid Water down to −37.5°C Using a Spectral Microphysics Model." *Geophysical Research Letters* 28.20 (2001): 3887. Print.

King, Michael D., Lawrence F. Radke, and Peter V. Hobbs. "Optical Properties of Marine Stratocumulus Clouds Modified by Ships." *Journal of Geophysical Research* 98.D2 (1993): 2729-739. Print.

Lindsey, Daniel T., and Louie Grasso. "An Effective Radius Retrieval for Thick Ice Clouds Using GOES." *Journal of Applied Meteorology and Climatology* 47.4 (2008): 1222-231. Print.

Lindsey, Daniel T., Donald W. Hillger, Louie Grasso, John A. Knaff, and John F. Dostalek. "GOES Climatology and Analysis of Thunderstorms with Enhanced 3.9-m Reflectivity." *Monthly Weather Review* 134.9 (2006): 2342-353. Print.

Ludlam, F. H. *Severe Local Storms: A Review*. Vol. 27. N.p.: American Meteorological Society, 1963. Print.

Menzel, W. Paul, and James F. W. Purdom. "Introducing GOES-I: The First of a New Generation of Geostationary Operational Environmental Satellites." *Bulletin of the American Meteorological Society* 75.5 (1994): 757-81. Print.

Menzel, W. Paul. "Radiometer Design Considerations." *Remote Sensing Applications with Meteorological Satellites*. Madison, WI: NOAA Satellite and Information Service, University of Wisconsin--Madison, 2006. 216-25. Print.

Moller, Alan R., Charles A. Doswell, III, Michael P. Foster, and Gary R. Woodall. "The Operational Recognition of Supercell Thunderstorm Environments and Storm Structures." *Weather and Forecasting* 9 (1994): 327-47. Print.

Mueller, Cynthia K., and Richard E. Carbone. "Dynamics of a Thunderstorm Outflow." *Journal of the Atmospheric Sciences* 44 (1987): 1879-898. Print.

Nakajima, Teruyuki, and Michael D. King. "Determination of the Optical Thickness and Effective Particle Radius of Clouds from Reflected Solar Radiation Measurements. Part I: Theory." *Journal of the Atmospheric Sciences* 47.15 (1990): 1878-893. Print.

"NWS Weather Fatality, Injury and Damage Statistics." *National Weather Service Office of Climate, Water and Weather Services*. National Oceanographic and Atmospheric Administration, 25 Sept. 2012. Web. 9 Oct. 2012. <http://www.nws.noaa.gov/om/hazstats.shtml>.

Pavolonis, Michael J., Andrew K. Heidinger, and Taneil Uttal. "Daytime Global Cloud Typing from AVHRR and VIIRS: Algorithm Description, Validation, and Comparisons." *Journal of Applied Meteorology* 44.6 (2005): 804. Print.

Polger, Paul D., Barry S. Goldsmith, Richard C. Przywarty, and Joseph R. Bocchieri. "National Weather Service Warning Performance Based on the WSR-88D." *Bulletin of the American Meteorological Society* 75.2 (1994): 203-14. Print.

Rockel, B., E. Raschke, and B. Wayres. "A Parameterization of Broad Band Radiative Transfer Properties of Water, Ice and Mixed Phase Clouds." *Beitraege Zur Physik Der Atmosphaere* 64.Feb (1991): 1-12. Print.

Rodgers, C. D. "Inverse Methods for Atmospheric Sounding: Theory and Practice." *World Scientific* (2000): n. pag. Print.

Rosenfeld, Daniel, and Itamar M. Lensky. "Satellite–Based Insights into Precipitation Formation Processes in Continental and Maritime Convective Clouds." *Bulletin of the American Meteorological Society* 79.11 (1998): 2457-476. Print.

Rosenfeld, Daniel, and William L. Woodley. "Deep Convective Clouds with Sustained Supercooled Liquid Water down to -37.5 C." *Nature* 405 (2000): 440-42. Print.

Ryzhkov, Alexander V., Terry J. Schuur, Donald W. Burgess, and Dusan S. Zrnic. "Polarimetric Tornado Detection." *Journal of Applied Meteorology* 44.5 (2005): 557. Print.

Sieglaff, Justin M., Lee M. Cronce, Wayne F. Feltz, Kristopher M. Bedka, Michael J. Pavolonis, and Andrew K. Heidinger. "Nowcasting Convective Storm Initiation Using Satellite Based Box-Averaged Cloud Top Cooling and Cloud Type Trends." *Journal of Applied Meteorology and Climatology* 50 (2010): 110-26. Print.

"Storm Prediction Center Severe Weather Summaries." *Storm Prediction Center Severe Weather Summaries*. National Oceanographic and Atmospheric Administration, n.d. Web. 09 Oct. 2012. <http://www.spc.noaa.gov/climo/online/>.

Sun, Juanzhen, and Ying Zhang. "Analysis and Prediction of a Squall Line Observed during IHOP Using Multiple WSR-88D Observations." *Monthly Weather Review* 136.7 (2008): 2364-388. Print.

"Thunderstorm Hazards - Hail." *NWS JetStream*. National Weather Service, 2 May 2011. Web. 09 Oct. 2012. <http://www.srh.noaa.gov/jetstream/tstorms/hail.htm>.

Walther, Andi, and Andrew K. Heidinger. "Implementation of the Daytime Cloud Optical and Microphysical Properties Algorithm (DCOMP) in PATMOS-x." *Journal of Applied Meteorology and Climatology* (2012): n. pag. Print.

Walther, Andi, William Straka, and Andrew K. Heidinger. *ABI Algorithm Theoretical Basis Document for Daytime Cloud Optical and Microphysical Properties (DCOMP)*. ATBD. 2nd ed. N.p.: NOAA NESDIS Center for Satellite Applications and Research, 2010. Print.

Wang, Pao K. "The Wisconsin Dynamic/Microphysical Model (WISCDYMM) and the Use of It to Interpret Satellite-Observed Storm Dynamics." *Measuring Precipitation from Space: EURAINSAT and the Future*. Ed. Vincenzo Levizzani, Peter Bauer, and F. Joseph. Turk. Dordrecht, the Netherlands: Springer, 2007. 435-46. Print.

Zipser, Edward J. "Deep Cumulonimbus Cloud Systems in the Tropics with and without Lightning." *Monthly Weather Review* 122.8 (1994): 1837-851. Print.